chemosensors

Review

Metal Oxide Semiconductor Gas Sensors for Lung Cancer Diagnosis

Guangyao Li, Xitong Zhu, Junlong Liu, Shuyang Li and Xiaolong Liu *

School of Materials, Sun Yat-sen University, Shenzhen 518107, China
* Correspondence: liuxlong9@mail.sysu.edu.cn

Abstract: Lung cancer is the most prevalent severe illness in both sexes and all ages and the leading cause of cancer-related deaths globally. Late-stage diagnosis is the primary cause of its high mortality rate. Therefore, the management of lung cancer needs early-stage screening. Breath analysis is a non-invasive, low-cost, and user-friendly approach to diagnosing lung cancer. Among the various types of breath sensors, MOS gas sensors are preferred due to their high gas responses, fast response times, robustness, and lower price. This review focuses on the critical role of MOS gas sensors in detecting VOCs in lung cancer patients' exhaled breath. It introduces the basic working mechanism of MOS gas-sensitive materials, summarizes some high-performance MOS materials suitable for detecting potential lung cancer biomarkers and provides performance enhancement strategies. The review also briefly introduces the sensor array and its pattern recognition algorithm. Finally, we discuss the challenges in developing MOS gas sensors for lung cancer screening and present the prospect of using the e-nose for large-scale early lung cancer screening.

Keywords: MOS gas sensor; lung cancer diagnosis; sensor array; exhaled breath VOCs

check for updates

Citation: Li, G.; Zhu, X.; Liu, J.; Li, S.; Liu, X. Metal Oxide Semiconductor Gas Sensors for Lung Cancer Diagnosis. *Chemosensors* **2023**, *11*, 251. https://doi.org/10.3390/chemosensors11040251

Academic Editor: Pi-Guey Su

Received: 2 March 2023
Revised: 4 April 2023
Accepted: 13 April 2023
Published: 17 April 2023

Copyright: © 2023 by the authors. Licensee MDPI, Basel, Switzerland. This article is an open access article distributed under the terms and conditions of the Creative Commons Attribution (CC BY) license (https://creativecommons.org/licenses/by/4.0/).

1. Introduction

Cancer incidence and mortality rates have risen rapidly worldwide, making it a significant cause of death for the global population [1,2]. The latest global cancer statistics report, "*Global Cancer Statistics 2020*", evaluated data on 36 major cancers from 185 countries or regions worldwide, revealing nearly 19.3 million new cancer cases in 2020, with lung cancer accounting for over 2.2 million cases and approximately 1.8 million deaths [2]. Of all cancer types, lung cancer has the highest mortality rate of 18%, posing a severe threat to human health and life (Figure 1). The five-year survival rate for lung cancer patients is only approximately 15% [3], with the prognosis varying significantly based on the clinical stages [4,5]. The TNM (tumor-node-metastasis) staging system (version 8) suggests that early-stage I lung cancer patients can achieve a five-year survival rate of over 70% after surgical treatment, while late-stage IV lung cancer patients remain below 10%, even with adequate treatment [4]. Early diagnosis and treatment are critical to improving the prognosis of lung cancer patients [6]. However, early lung cancer rarely exhibits clinical symptoms, and nonspecific symptoms are the leading cause of obtaining a lung cancer diagnosis [7–9]. As a result, lung cancer is often diagnosed in late-stage, and the cancer tissue has already metastasized from the primary site, indirectly leading to the high mortality rate of lung cancer [10]. Therefore, active screening is crucial in diagnosing early-stage lung cancer, significantly reducing treatment pain, improving survival rates, and avoiding the high costs of late-stage treatment.

Currently, clinical lung cancer diagnosis mainly relies on sputum cytology examination [11,12], histopathological examination [13–15], and imaging examination [16–21]. Sputum, secreted from the lungs, bronchi, and trachea, can carry pathological information when these areas are diseased [11,12]. Despite its simplicity and low equipment requirements, a cytology examination of exfoliated cells in the sputum is limited by its identification of cell morphology and high false positive rate, which depends on the quality of the sputum specimens and physician experience [12]. Histopathological examination, obtained through percutaneous puncture lung sampling, provides a reliable lung cancer diagnosis with high diagnostic accuracy and staging confirmation [15]. However, histopathological examination is typically conducted after a lesion has formed due to its high invasiveness and reliance on accurate localization, rendering it unsuitable for early screening in high-risk populations. Bronchoscopy can visualize the lesion location and provide a qualitative diagnosis by inserting a fiberoptic probe into the bronchus, but it is limited by the probe's reach and observation range and is unsuitable for early lung cancer screening due to the difficulty of seeing early lesions under the mucosa [13,14]. Imaging examination using CXR (Chest X-ray), CT (computed tomography), and PET (positron emission computed tomography) has become a commonly used early lung cancer screening method to quickly and non-invasively examine specific areas to show the position, size, and shape of the tumors. However, each modality has limitations, such as CXR's limited resolution for detecting only larger lumps (greater than 10 mm) [16] and LDCT's (low-dose CT) higher false positive rate [17–19]. PET has high sensitivity and specificity for early-stage lung cancer diagnosis but is costly, making it challenging to be popularized in large-scale routine examinations [20,21]. Additionally, radiation exposure is a practical concern in all imaging examinations.

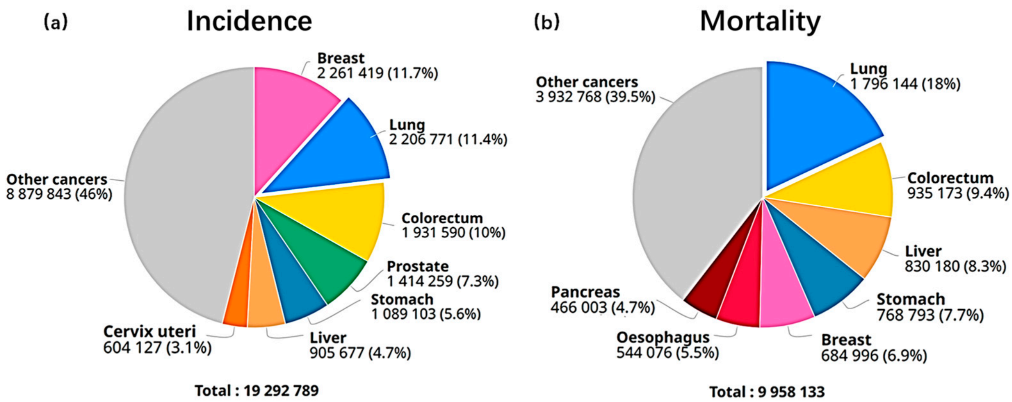

Figure 1. Global major cancer statistics (in 2020, the world, both sexes, all ages). (**a**) The type, number, and proportion of new cancer cases; (**b**) the type, number, and proportion of cancer deaths. Reproduced with permission from Ref. [2], © 2021 American Cancer Society.

Breathing is the physiological gas exchange process between the human body and the external environment. The human metabolism generates various volatile organic compounds (VOCs) that can pass through the bloodstream to the alveoli and exhale via respiration. As such, the VOC composition in exhaled breath can indicate human metabolism and health status [22]. Consequently, by detecting and analyzing the components of exhaled breath to identify lung cancer biomarkers, exhaled breath analysis is a promising tool for early lung cancer screening [23–26]. Compared to conventional lung cancer diagnostic methods, exhaled breath analysis is non-invasive, convenient, and provides rapid and accurate results [27,28].

As early as the 1970s, Pauling et al. employed gas chromatography (GC) to identify approximately 250 VOCs in the exhaled breath of healthy individuals [29]. Since then, advances in detection methods have led to identifying a more significant number of VOCs. Using gas chromatography–mass spectrometry (GC–MS), Phillips et al. detected 3481 VOCs in exhaled breath samples from 50 healthy subjects, of which only 27 VOCs were found in all subjects [30]. The study revealed that acetone, isoprene, ethanol, methanol, and 2-propanol were the major VOCs in exhaled breath, with 2-propanol being considered exogenous due to its similar concentration in exhaled breath and ambient air [31,32]. Inorganic gases, such as N_2, O_2, CO_2, and H_2O, are the main components in exhaled breath, potentially interfering with identifying VOCs [32]. These findings indicate that the exhaled breath composition is complex, and identifying VOCs as lung cancer biomarkers remains challenging.

In 1985, Gordon et al. first used GC–MS to analyze the exhaled breath samples of 17 healthy individuals and 12 lung cancer patients and found 22 VOCs that differed between the two groups. They first proposed using exhaled breath for lung cancer diagnosis [26]. Subsequently, Phillips' team discovered that the exhaled breath of lung cancer patients contained significantly more alkanes and emphasized the potential of VOCs in exhaled breath for lung cancer diagnosis [33–35]. Additionally, they developed nonlinear multivariate analysis methods that improved the ability to diagnose lung cancer by utilizing different combinations of VOCs in exhaled breath [36,37]. O-toluidine [38], toluene [39], and 1-propanol [40] were commonly regarded as VOC biomarkers for lung cancer, as their concentrations were found to be significantly higher in the exhaled breath of lung cancer patients than in that of healthy individuals. Koureas et al. found a strong correlation between the presence of ethylbenzene, toluene, styrene, 2-propanol, and 1-propanol in exhaled breath and the ability to distinguish between cancer patients and healthy individuals [41]. Schallschmidt et al. quantified the concentration of 24 potential VOC biomarkers for lung cancer [42]. They found that the concentration of aromatic compounds in the exhaled breath of smokers increased. In contrast, the oxygen-containing VOC concentration in lung cancer patients' exhaled breath increased significantly, such as aldehydes, 2-butanone, and 1-butanol. The production of these VOCs may be related to the oxidative stress behavior of lung cancer cells caused by excessive free radicals and reactive oxygen species (ROS) in the cells of lung cancer patients [43–45].

Figure 2 summarizes the hypothetical basis for generating different types of VOC biomarkers in the exhaled breath of lung cancer patients [46]. During oxidative stress, ROS can cause oxidative DNA damage, polyunsaturated fatty acids (PUFAs), proteins, and other substances in the body, while also generating volatile hydrocarbons and aldehydes, which excrete through respiration [46–48]. Exposure to carcinogens (such as cigarette smoke, benzene, and nitrosamines) can increase the risk of cell carcinogenesis by causing ROS accumulation. It induces changes in cytochrome P450 enzyme activity patterns, generating VOC biomarkers for lung cancer [46]. The Warburg effect, resulting from the prompt proliferation of lung cancer cells in a hypoxic condition, is another possible source of VOC biomarkers [49]. At this time, glycolysis activity is higher than oxidative phosphorylation, increasing the metabolites of glycolysis, such as acetaldehyde, ethanol, and acetone, in exhaled breath [50,51].

However, there is no consensus on lung cancer biomarkers in exhaled breath due to the variations in breath sampling methods, gas detection technologies, and patient factors (including lung cancer type, body weight, and dietary habits) [52–54]. Jia et al. compared the VOC types in exhaled breath from lung cancer patients and the in vitro lung cancer cell cultures and discussed the methodological issues that may cause inconsistencies between studies. They suggested that potential VOC biomarkers for lung cancer may include 1-propanol, isoprene, acetone, pentane, hexanal, benzene, toluene, and ethylbenzene [55]. Schmidt et al. reviewed research on the exhaled breath biomarkers for lung cancer over the past four decades and proposed using frequently studied VOCs as potential biomarkers [56]. Figure 3 shows some of the most common VOCs identified as lung cancer biomarkers, including BTEX (benzene, toluene, ethylbenzene, and xylene), isoprene, hexanal, nonanal, 2-butanone, acetone, pentane, and 1-propanol [56]. Notably, no VOCs have been identified that are exclusively present in exhaled breath from lung cancer patients [42,57].

In order to assess the reliability of the diagnostic methods utilizing exhaled breath, researchers have employed machine learning and selected various combinations of potential lung cancer VOCs to build prediction models [8,41,53,58]. For example, Chen et al. developed a model comprising 20 VOCs that achieved 93.9% accuracy in distinguishing between non-small cell lung cancer (NSCLC) and small cell lung cancer (SCLC), and another model composed of 19 VOCs that could differentiate between early and late-stage lung cancer with an accuracy of 82.7% [8]. Nevertheless, the most prevalent method used for exhaled breath diagnosis entails the application of large instruments such as GC–MS. While effective in detecting low-concentration VOCs, they have limitations, such as complexity, high costs, and lack of portability, hindering their widespread use in routine home check-ups. Furthermore, they cannot provide real-time analysis. In a prospective study, Peled et al. used GC–MS and a gas sensor to detect the exhaled breath in 72 patients with lung nodules, and the latter selectively distinguished between benign and malignant nodules via pattern recognition, even successfully differentiating between two different types of lung cancer (adenocarcinoma and squamous cell carcinoma) [54], indicating that gas sensors have the potential to become low-cost, small, portable exhaled breath detection and analysis devices. Advanced gas sensors have been developed for low-concentration gas detection in recent years [54,59–65], including surface acoustic wave (SAW) sensors, quartz crystal microbalance (QCM) sensors, electrochemical gas sensors, and oxide semiconductor (MOS) gas sensors. In particular, the MOS gas sensors have made them a promising alternative for VOC detection due to their small size, low cost, fast response, and sensitivity in low-concentration (ppt levels) gases [48,66].

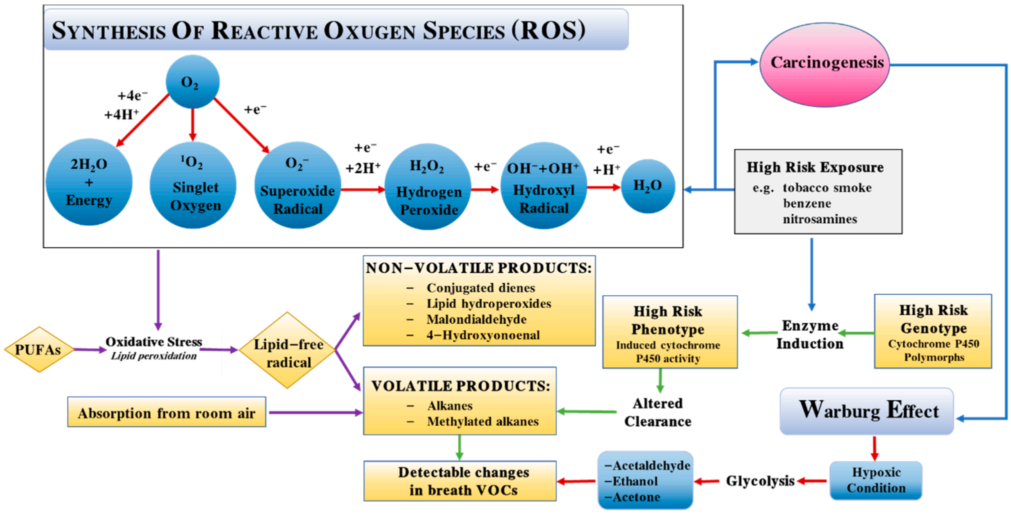

Figure 2. Hypothetical basis of the breath test for lung cancer. Lung cancer may result from the interaction of hereditary and environmental factors. Several cytochrome P450 mixed oxidases are activated by exposure to environmental toxins such as tobacco smoke. The induced phenotype may increase the risk of lung cancer by increased conversion of precursors to carcinogens. An altered pattern of cytochrome P450 mixed oxidase activity could modulate the catabolism of endogenous VOCs products of oxidative stress and generate an altered pattern of breath VOCs. The Warburg effect is another possible source of VOCs in the exhaled breath associated with glycolysis in a hypoxic condition.

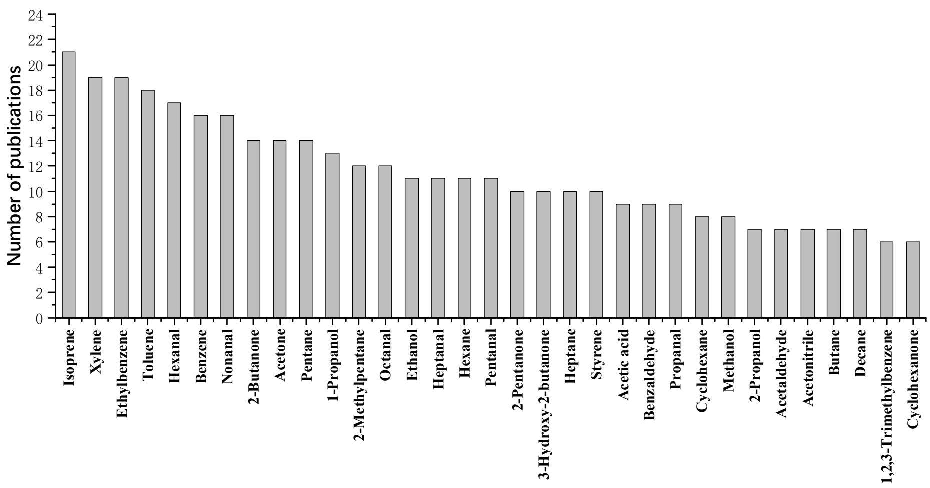

Figure 3. VOCs are most often noted as lung cancer biomarkers in exhaled breath.

Many reviews about applying MOS gas sensors in exhaled breath disease diagnosis exist. These studies have focused on various aspects, such as identifying a single gas (such as acetone) [67,68], developing sensor devices [69,70], utilizing MOS materials with special structures (such as MOF) [71,72], and improving sensitivity and selectivity [73]. However, despite the potential of MOS gas sensors in detecting VOCs in exhaled breath [60–62], there is currently no universal marker for lung cancer. Considering the urgency for early lung cancer diagnosis and the significant potential of MOS gas sensors in this area, it is necessary to review the recent progress in this field. This review summarizes the latest research on MOS gas sensors in lung cancer diagnosis, including their working mechanisms, candidate MOS materials, and the current research progress of MOS sensor arrays. We also discuss the challenges in developing MOS gas sensors for early lung cancer screening.

2. MOS Gas Sensor for Lung Cancer Biomarker VOCs

MOS gas sensors are highly regarded for their high sensitivity, fast response, simple fabrication, durability, small size, and easy integration [48,74]. The origin of semiconductor gas-sensitive materials dates back to 1931 when Engelhard et al. discovered that the conductivity of Cu_2O changed with water vapor adsorption. Despite this finding, it received little attention [75]. In 1962, Seiyama et al. first observed the distinct resistance of ZnO thin films in combustible gases and air at high temperatures, establishing the foundation for MOS gas sensors [74]. Since then, MOS gas sensors have evolved rapidly, with the first commercial MOS gas sensor developed in 1968. To satisfy the requirements of MOS gas sensors in complex environments, Persaud et al. proposed a method of mimicking the animal olfactory system (e-nose) in 1982 to improve the selectivity of sensors for VOCs by using an array of MOS materials with different characteristics to detect mixed gases concurrently [76]. In the following decades, the gas-sensitive mechanism of MOS was further explored [77–80], the gas sensitivity of a single MOS was continuously enhanced [81], and the fabrication methods of sensor arrays and analysis algorithms were constantly being improved [82,83].

2.1. Working Mechanism

The working mechanism of MOS gas sensors depends on the sensing material's conductivity change when exposed to different gas environments, enabling target gas detection. Several theories, including the chemisorbed oxygen model [78], the grain boundary barrier model [79], the bulk resistance model [84], and the space-charge layer model (electron depletion layer (EDL) and hole-accumulation layer (HAL)) [77,80], can explain the MOS conductivity changes. The key to these theories is the interaction between the gas and material surfaces [85]. When the affinity energy of the gas molecules exceeds the work function of the MOS surface, electrons transfer from the MOS surface to the gas molecules, resulting in gas anions forming and being adsorbed onto the MOS surface [86]. In particular, the chemisorbed oxygen species ($O_2{}^-$, O^-, O^{2-}) play a crucial role in MOS surface conductivity [78]—closely related to the working temperature and MOS type—determining the MOS's gas-sensing properties [87–89]. The formation process of chemisorbed oxygen species on the surface of SnO_2 can be summarized by the following formulas [89] (Formulas (1)–(4)). We should note that MOS gas sensors have a broad response mode, leading to low selectivity, which can be improved by compounding them with other types of materials [90].

$$\mathrm{Inair}: \mathrm{O_2(gas)} \rightarrow \mathrm{O_2(abs)} \tag{1}$$

$$\mathrm{T} < 150\ ^\circ\mathrm{C}: \mathrm{O_2(abs)} + e^- \rightarrow \mathrm{O_2^-(abs)} \tag{2}$$

$$150\ ^\circ\mathrm{C} < \mathrm{T} < 400\ ^\circ\mathrm{C}: \mathrm{O_2^-(abs)} + e^- \rightarrow 2\mathrm{O^-(abs)} \tag{3}$$

$$T > 400\ ^\circ C : O^-(abs) + e^- \rightarrow O^{2-}(abs) \quad (4)$$

For n-type SnO_2, the gas–surface interaction process can be explained as follows (Figure 4) [85,86]. Firstly, O_2 in the air is adsorbed onto the oxygen adsorption site on the SnO_2 surface when heated to a specific temperature. Subsequently, oxygen molecules capture the conduction band electrons of MOS to form chemisorbed oxygen species ($O_2{}^-$, O^-, O^{2-}) and simultaneously create an EDL at the MOS grain contact interface, which results in a higher barrier, increasing the resistance. When introducing a reducing gas such as ethanol, the gas reacts with the chemisorbed oxygen species and releases the electrons back into the MOS simultaneously, thus lowering the resistance. These oxygen species can desorb or be adsorbed again onto the MOS surface to create new oxygen anions. On the other hand, introducing an oxidizing gas will further deplete the sensing layer electrons and increases MOS resistance.

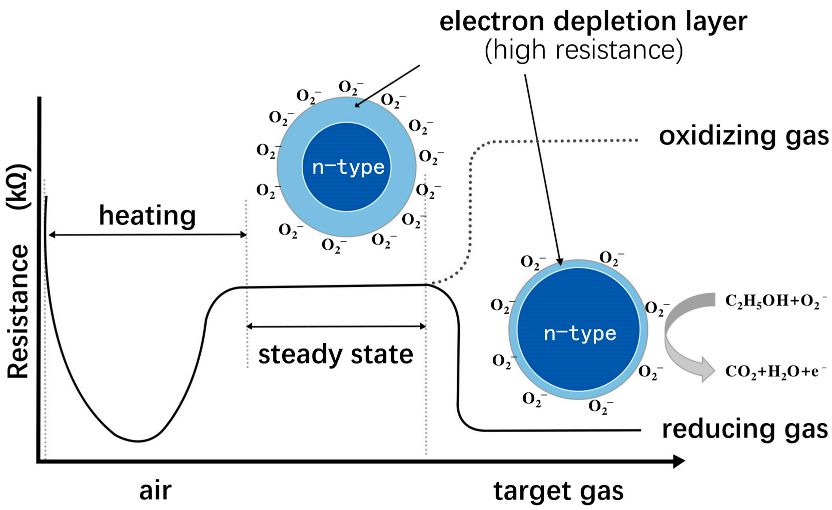

Figure 4. Schematic diagram of detection principle of n-type MOS sensitive material.

Although there is no unified theory on gas-sensing mechanisms, rational experimental designs based on existing materials can enhance their gas-sensing properties. The width of the space-charge layer, also known as the Debye length, typically ranges from 2 to 100 nm due to oxygen adsorption on the MOS surface. When the MOS grain size is close to or less than twice the Debye length, it amplifies the sensitivity considerably, demonstrating the remarkable potential of nanomaterials in gas sensors [91]. Nevertheless, excessively small particle sizes can cause nanoparticle aggregation, which will hinder the participation of internal particles in the reaction and decrease the gas-sensing properties of MOS [72]. Hence, specific nanoscale structural designs are necessary to reduce particle size while preventing nanoparticle aggregation. The heterojunction effect and synergistic effect can also impact the gas-sensing properties of MOS materials [92], which can be achieved through metal ion doping, metal particle modification, and compounding with other substances on the MOS substrate. In summary, the micro/nanostructure design and "second-phase modification" are essential methods for enhancing the gas-sensing properties of MOS materials. However, designing a new gas-sensitive material from scratch is still challenging.

2.2. Candidate Materials

Early comments on gas sensor design suggested that any sufficiently fine dispersed metal oxide could serve as a gas-sensitive layer for gas sensors, regardless of the practical usage requirements [93]. However, the exhaled gas of humans contains many components with low concentrations [30,32], making it necessary to identify the most appropriate candidate material among a wide range of available materials to accurately and efficiently measure the components and concentrations of exhaled breath [94]. We conducted a search using keywords such as "material name", "chemical formula", and "gas sensor" to investigate the most researched MOS over the past few decades. For the n-type semiconductors SnO_2, ZnO, TiO_2, WO_3, In_2O_3, Fe_2O_3, and CeO_2, the number of search results was 12,663, 10,920, 5269, 4102, 3487, 2643, and 1012, respectively, while for the p-type semiconductors CuO, NiO, Co_3O_4, Cr_2O_3, and Mn_3O_4, they were 3003, 2649, 1604, 822, and 564, respectively. The statistics show in Figure 5 that the overall proportions of the research results for the n-type and p-type MOS gas-sensitive materials were 82.3% and 17.7%, respectively. Among the top five materials, SnO_2, ZnO, TiO_2, WO_3, and In_2O_3 were n-type MOS materials, indicating that more attention has been paid to the research and development of n-type MOS gas-sensitive materials. According to Hübner et al., the inherent low sensitivity of p-type MOS materials restricts their development [95]. Furthermore, only TiO_2 belongs to the bulk resistance-controlled MOS among the top five materials. The conductivity change in them involves the reaction of gas with the lattice oxygen of the material, leading to a higher reaction temperature (usually above 700 °C), slower response rate, and poorer stability, making it less suitable for the detection of VOCs in exhaled breath [96–99].

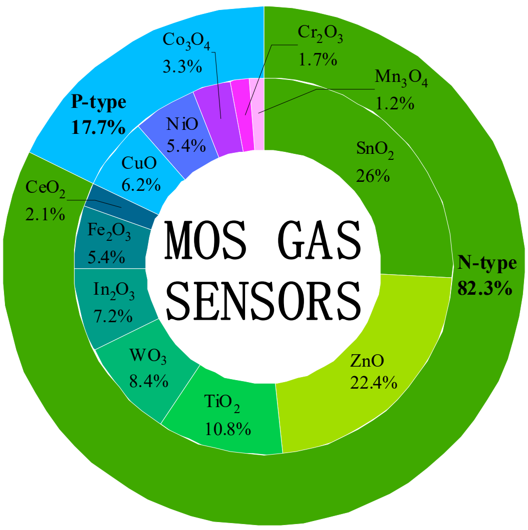

Figure 5. Publication of papers and patents on major MOS gas sensors before 15 February 2023. Here, the papers and patents were searched on the Web of Science, refined by 'keywords = gas sensor, the chemical formula and the scientific name of the sensor material' with all document types on 15 February 2023.

According to the statistical analysis of exhaled breath biomarkers for lung cancer VOCs and MOS gas-sensing materials (Figures 3 and 4), the n-type surface resistivity-controlled MOS materials have gained significant attention for detecting VOCs in exhaled breath for lung cancer diagnosis. Among them, SnO_2 and ZnO are currently the two most widely studied MOS gas-sensing materials and receive the most attention. Therefore, the following sections will focus on the latest research on n-type MOS gas-sensing materials (especially SnO_2 and ZnO), detecting exhaled breath biomarkers of lung cancer (BTEX, isoprene, hexanal, nonanal, 2-butanone, acetone, n-pentane, 1-propanol, etc.), considering the diverse types, low concentrations, and high-humidity conditions of exhaled breath analysis. The aim is to guide the development of e-nose devices with higher sensitivity, better selectivity, and more excellent stability to enable early lung cancer screening on a large scale.

2.3. Single MOS Gas Sensor and Performance Improvement Strategy

BTEX, comprising benzene, toluene, ethylbenzene, and xylene, has been frequently detected in the exhaled breath of lung cancer patients [56], as demonstrated by the statistical data presented in Figure 3. These compounds are metabolized similarly in lung cancer patients and are often detected together in exhaled breath samples [46,56]. However, due to the limited selectivity of MOS gas sensors for VOCs in this family, it is advisable to select one of the strongly correlated BTEX gases as a representative for detection [100]. For instance, the toluene content in the exhaled breath of lung cancer patients is approximately 2–3 times higher than that of healthy individuals, ranging from 80 to 100 ppb [101].

When evaluating the performance of MOS gas-sensing materials for detecting lung cancer exhaled breath biomarkers, several parameters should be considered beyond sensitivity and response time. In particular, the selectivity, limits of detection (LOD), and stability are significant. Selectivity refers to a gas sensor's ability to detect the target gas in the presence of other gases, which is crucial, given that over 3000 VOCs and various inorganic gas matrices are in human exhaled breath [30,32,102]. LOD refers to the lowest target gas concentration corresponding to the gas sensor's minimum reliable response sensitivity value. MOS sensors should exhibit high sensitivity to detect low-concentration (ppt levels) VOCs [25,103]. Stability means the ability of MOS sensors to obtain reliable results over time, which is essential for an accurate diagnosis [104].

2.3.1. Structures and Gas-Sensing Performance

The gas-sensing properties of MOS are significantly affected by its morphology and size [72,91]. A general strategy to enhance its performance is to optimize its structure and morphology, which can lead to a high specific surface area and excellent chemical activity [91,105]. SnO_2 is the most widely studied material in MOS gas sensors [106] due to its exceptional stability and electron transfer ability [107] (as shown in Figure 4). As a surface resistance-controlled MOS, SnO_2 provides abundant surface chemical properties owing to its bivalent states of tin elements (i.e., Sn^{4+} and Sn^{2+}), making it more tunable than other univalent MOSs [108,109]. To date, various SnO_2 morphologies have been developed, such as nanoparticles [110], nanospheres [111], nanowires [112,113], nanotubes [114], nanofilms [115], nanosheets [116,117], and 3D nanostructures [118–121].

Figure 6a,b shows two schematic diagrams of the synthesis route of multi-layer SnO_2, respectively. Bing et al. successfully synthesized SnO_2 with a yolk-shell cuboctahedra porous structure formed by self-assembled nanoparticles (Figure 6a); the response to 20 ppm toluene was 28.6 at 250 °C, with short response/recovery times of 1.8 s and 4.1 s, respectively (Figure 6c) [120]. Compared with the solid cubes and single-shell structures of SnO_2 synthesized during the same period, the yolk-shell cuboctahedra structure of SnO_2 exhibited higher sensitivity and a shorter response/recovery time at the same concentration due to its loose and porous structure. This structure provides more active adsorption sites for gas–surface interactions and greater stability than the single-shell structure, thus promoting continuous gas–surface reactions. Wang et al. used a controllable multi-step synthesis method to obtain three-layer, double-layer, and single-layer hollow cubic SnO_2 samples at different experiment stages (Figure 6b). The gas-sensing test results for each at 20 ppm toluene at 250 °C showed that the responses were 38.7, 33.4, and 22.1, with corresponding response/recovery times of 0.8/6.1 s, 2.3/5.8 s, and 2.0/6.5 s, respectively (Figure 6d). It can be observed that the response of the sample enhanced with the number of layers in the hollow cubic structure. The three-layer hollow cubic structure of SnO_2 [113] exhibited a higher response value and a shorter response time compared to the "double-layer" yolk-shell cuboctahedra structured one [120] under similar testing conditions. This work demonstrates the significant promoting effect of multi-layer structures on the gas-sensing performance of SnO_2. However, the high LOD limits their application in detecting exhaled gas components in patients with lung cancer; thus, it is necessary to consider other methods to reduce the LOD.

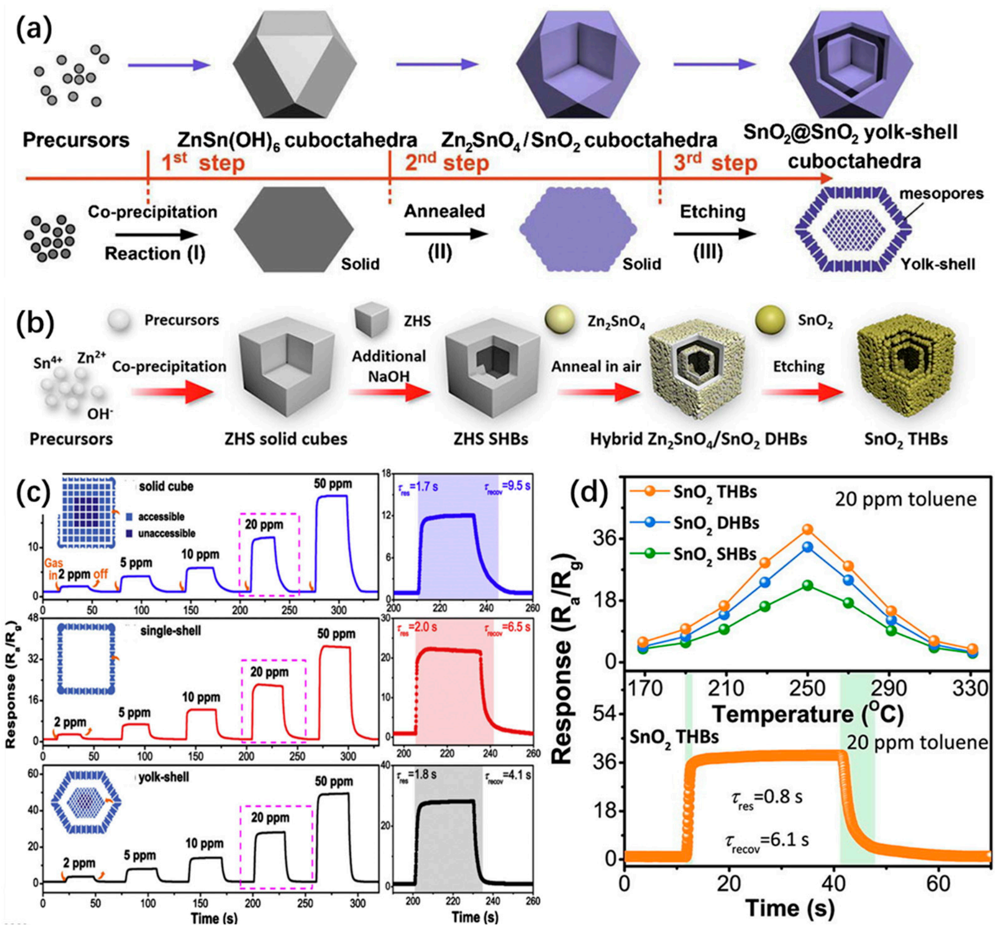

Figure 6. Structures and gas-sensing performance of SnO_2. Schematic illustration for the formation of (**a**) yolk-shell SnO_2 hollow structures and (**b**) SnO_2 THBs. (**c**) Dynamic sensing transients of three SnO_2 products to toluene with different concentrations. The right insets show the corresponding response time (τ_{res}) and recovery time (τ_{recov}) examined to 20 ppm toluene. (**d**) Response of sensors based on different SnO_2 nanostructures versus 20 ppm toluene concentration. The below part shows the τ_{res} and τ_{recov} examined to 20 ppm toluene for SnO_2 THBs. Panels (**a**,**c**): reproduced with permission from Ref. [120], © 2016 Elsevier B.V. Panels (**b**,**d**): reproduced with permission from Ref. [121], © 2020 Elsevier B.V.

2.3.2. Noble Metal Modification and Gas Sensing Performance

The surface modification of noble metals has proven to be an effective strategy for enhancing the response and selectivity of MOS gas sensors and reducing the operating temperature and response/recovery time [122]. It is worth noting that noble metal surface modification can be achieved through either chemical or electronic sensitization [79,123]. Chemical sensitization utilizes the catalytic effect of noble metal nanoparticles to directly boost the reaction rate between the target gas and chemisorbed oxygen [79]. In contrast, electronic sensitization indirectly enhances the gas sensor's performance by transferring electrons from the MOS to noble metal, thus providing more oxygen adsorption sites [123]. For example, Qiao et al. reported achieving a LOD of toluene below 100 ppb by loading Pd nanoparticles onto a SnO_2 monolayer nanocage (Figure 7d,e) [119]. Moreover, the 1%Pd-SnO_2 monolayer nanocage demonstrated superior gas-sensing performance to a larger surface area of three-layered hollow cubic SnO_2, where the response of 20 ppm toluene was 41.4 and the response time was 0.4 s at 230 °C [121]. These results demonstrate the significant role of noble metal loading in improving the gas-sensing performance of MOS, which is attributed to Pd nanoparticles' dramatic chemical and electronic sensitization properties (Figure 7a–e).

Suematsu et al. also investigated the potential of Pd-SnO_2 as a sensing layer in gas sensors, which has shown promising results [124]. They found that adding Pd to the original SnO_2 improved its catalytic activity and transformed its microstructure. Specifically, the addition of Pd converted densely packed SnO_2 nanoparticles (NPs) into SnO_2 nanoparticle clusters (CNPs), and Pd nanoparticles attached to the surface of SnO_2 CNPs to form Pd-SnO_2 CNPs (Figure 7f,h). The large pores (approximately 10 nm in radius) between the Pd-SnO_2 CNPs facilitate the adsorption and diffusion of toluene molecules inside, significantly shortening the response/recovery time (Figure 7g,i). The dual-action of Pd-loading significantly enhances the sensing performance of original SnO_2, allowing Pd-SnO_2 CNPs to respond well to toluene concentrations as low as 1 ppb. Furthermore, its LOD for toluene reaches 200 ppt, which far exceeds the detection limit requirements for exhaled breath detection. It is worth mentioning that they recently proposed modifying the heating pulse drive mode to improve the sensor response further, reducing the LOD of gas sensors for toluene to 7 ppt [125].

Selectivity is a crucial factor in assessing the performance of gas-sensitive materials. Numerous studies have demonstrated that incorporating noble metals can effectively enhance MOS's selectivity [114,126–130]. For instance, Moon et al. designed a dual-layer gas sensor comprising a SnO_2 sensing layer and an xRh-TiO_2 (x = 0.5, 1, and 2 wt%) catalytic layer that solely catalyzes aromatic compounds, resulting in a selective response to BTX (benzene, toluene, and o-xylene) at the ppb level just by adjusting the Rh content in the Rh-TiO_2 catalytic layer [129]. The response of the pure SnO_2 sensing layer and three xRh-TiO_2 dual-layer gas sensors to the 5 ppm mixed gas (benzene, toluene, o-xylene, ethanol, formaldehyde, and carbon monoxide) is illustrated in Figure 7j–m. Within the operating temperature range of 325–425 °C, the xRh-TiO_2/SnO_2 sensors selectively responded to BTX compared to the pure SnO_2 sensors. The specific response behaviors of each sensor varied based on the Rh content, which demonstrates the possibility of customizing the selectivity of aromatic compound sensors by adjusting the Rh content of the catalytic layer. The quantification of BTX in the mixed gas was achieved successfully by forming the above sensors into a sensor array, as shown in Figure 7n.

In addition, the study of noble metals in multi-layer MOS gas sensors is not limited to the catalytic layer's catalysis; it can also be used in the sensing layer. For example, Jeong et al. developed a CeO_2/Rh-SnO_2 dual-layer gas sensor in which CeO_2 acted as the catalytic layer, and Rh-SnO_2 acted as the sensing layer [130] (Figure 7q,r). They systematically investigated the effect of the type of MOS in the sensing layer (SnO_2, ZnO, In2O_3, and WO_3) and the type of noble metal loaded onto it (Pt, Rh, and Au) on the sensors' selectivity and achieved quantitative differentiation of BTEXS (benzene, toluene, ethylbenzene, xylene, and styrene) at the ppb level [130] (Figure 7s,t). Unlike the Rh-TiO_2 catalytic layer of Rh-TiO_2/SnO_2 [129], the CeO_2 catalytic layer of CeO_2/Rh-SnO_2 [130] catalyzes interfering gases other than aromatic compounds, thereby avoiding the cross-response of the MOS sensing layer to interfering gases.

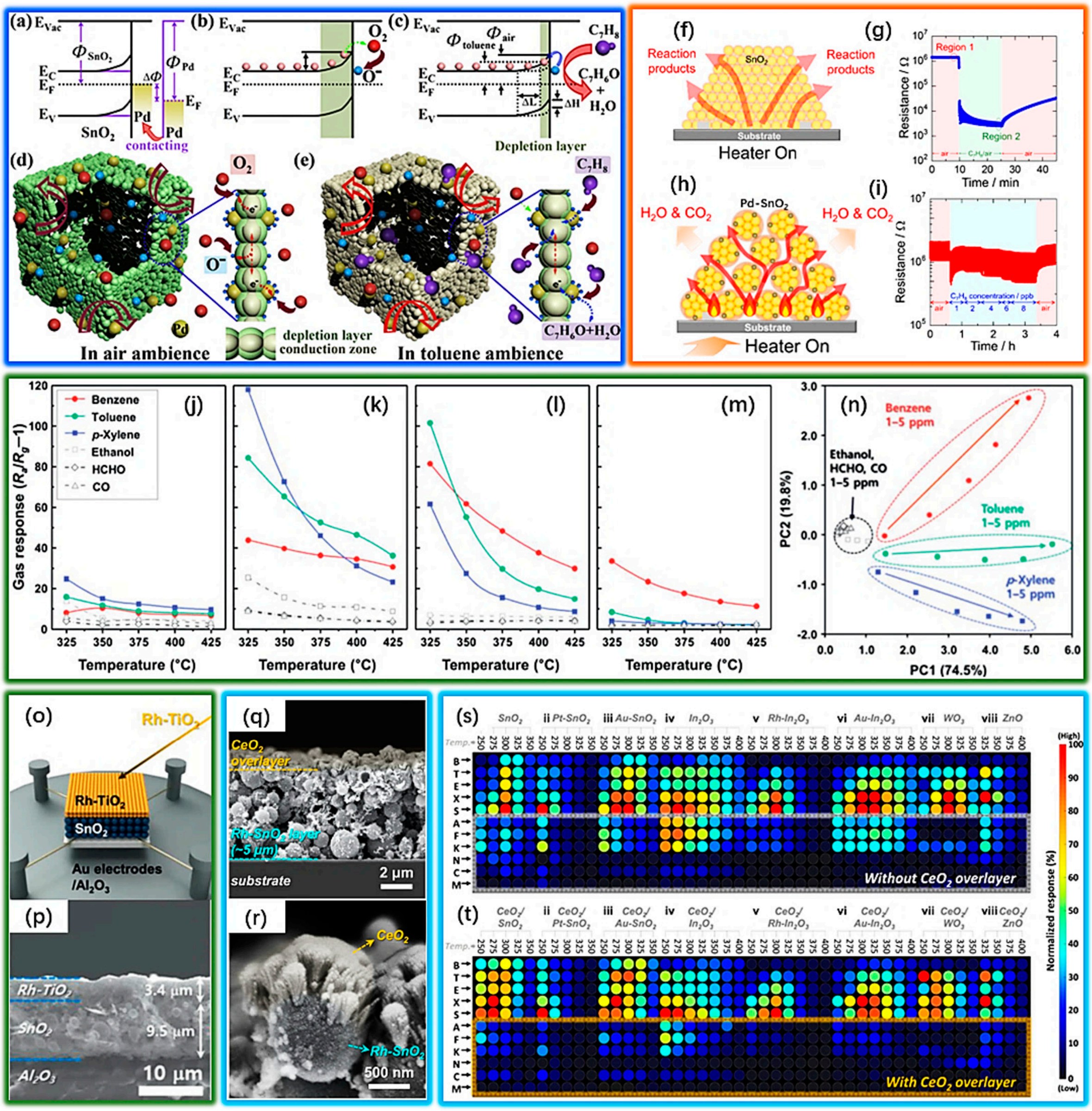

Figure 7. Noble metal modification and gas-sensing performance of SnO_2. Schematic energy band diagrams of a SnO_2 and Pd contact (**a**) with establishing the contact, with being exposed to (**b**) air and (**c**) toluene ambience, respectively. (**d**,**e**) Schematic diagrams of possible gas-sensing mechanisms of Pd-loaded SnO_2 porous cages. Schematic diagrams of the gas-diffusion behavior in (**f**) SnO_2 NPs and (**h**) Pd-SnO_2 CNPs. Transient response curve of the SnO_2 NPs microsensor to (**g**) 20 ppm toluene and (**i**) various toluene concentrations at an applied voltage of 1.04 V (~250 °C). Gas-sensing properties of (**j**) pure SnO_2, (**k**) 0.5Rh-TiO_2/SnO_2, (**l**) 1Rh-TiO_2/SnO_2, and (**m**) 2Rh-TiO_2/SnO_2 sensors to the 5 ppm mixed gases (benzene, toluene, *p*-xylene, ethanol, HCHO, and CO) within the operating temperature range of 325–425 °C. (**n**) PCA plot using the data from 0.5Rh-TiO_2/SnO_2, 1Rh-TiO_2/SnO_2, and 2Rh-TiO_2/SnO_2 sensors to demonstrate the discrimination of aromatic BTX compounds over the interferences from ethanol, HCHO, and CO (concentration: 1–5 ppm). (**o**) Schematic diagram of Rh-TiO_2/SnO_2 sensor. (**p**) Cross-sectional SEM image of Rh-TiO_2/SnO_2 sensing film. (**q**) Cross-sectional SEM and (**r**) FESEM images of CeO_2/Rh–SnO_2 film. (**s**,**t**) Normalized signal intensities of diverse single-layer sensors to 5 ppm analyte gases. Panels (**a**–**e**): reproduced with permission from Ref. [119], © 2016 Elsevier B.V. Panels (**f**–**i**): reproduced with permission from Ref. [124], © 2018 American Chemical Society. Panels (**j**–**p**): reproduced with permission from Ref. [129], © 2021 The Authors. Advanced Science published by Wiley-VCH GmbH. Panels (**q**–**t**): reproduced with permission from Ref. [130], © 2023, The Author(s).

2.3.3. Improve the Humidity Resistance

The sensitivity of MOS gas sensors will decrease when operating in a high-humidity environment, resulting from "water poisoning" [131]. Such degradation is a major limitation to the reliability of gas sensors [104]. The primary mechanism involves the reaction of H_2O with the chemisorbed oxygen species on the MOS surface, forming inert hydroxyl groups at the oxygen-active site. This alteration significantly impacts the MOS gas-sensing properties [79,104,132–134] and gas diffusion [135]. Moreover, water vapor is an unavoidable and substantial interference gas for MOS in exhaled breath detection. Researchers have concentrated on improving the material's humidity resistance to mitigate this issue.

The basic principle of eliminating the humidity's effect is to suppress the formation of hydroxyls on the MOS surface or increase oxygen vacancies to mitigate the impact of hydroxyls. A practical approach is to avoid the connection between H_2O and the active sites on the MOS surface. Some researchers have used strong hydrophilics, such as CuO, to composite with MOS to block the interaction between H_2O and the MOS surface. CuO/SnO_2 [136] and CuO/In_2O_3 [137] have shown excellent humidity resistance (Figure 8a,b). Bulemo et al. reported a porous Pt-loaded SnO_2 nanotube based on SiO_2, which exhibited excellent sensing performance under high humidity (95% RH), attributing to the residual SiO_2 responsible for strong humidity adsorption [114]. Low-valence doping is another method typically carried out in MOS to provide oxygen vacancies to improve humidity resistance [131,138]. Kwak et al. doped Tb on the surface of yolk-shell sphere SnO_2, which demonstrated a comparable response and resistance in dry and humid environments (Figure 8c) [131]. This compensating effect can be attributed to substituting Tb^{3+} for Sn^{4+} in SnO_2, which creates oxygen vacancies. However, the humidity resistance capacity obtained by the additive materials is limited.

Another strategy for improving MOS's humidity resistance is to enhance its hydrophobicity. Zhu et al. deposited a few nanometers-thick hydrophobic inorganic CeO_2 layer on SnO_2 thin film by magnetron sputtering to prepare the CeO_2/SnO_2 heterojunction film, making the material humidity resistant without being limited by other conditions (Figure 8d,e) [139]. However, the gas sensitivity of MOS is inevitably inhibited due to the hydrophobic layer covering its active sites. Jeong et al. developed a dual-layer sensor with a Tb_4O_7 coverage layer, which proved the universal humidity resistance effectiveness while maintaining a gas response, selectivity, and resistance (Figure 8f–k) [140]. The synthesis of surface-decorating materials requires additional materials and steps, increasing the complexity and cost of the process.

Microscopic morphology modification has also been proven to be an effective method for enhancing the humidity resistance of a single material [141]. Vallejos et al. fabricated ZnO thin films with rod- and needle-like structures (Figure 8l,m) [142]. Both ZnO structures show hydrophobicity, with static water contact angles (CA) of 120° and 134°, respectively, and maintain stable response values when only the humidity changes, indicating their excellent humidity resistance. The needle-like ZnO film with a larger contact angle has more excellent humidity resistance because it exposes more low-energy {100} facets, suggesting its lower reactivity to water. This specific morphology preparation method provides a novel approach to enhancing the humidity resistance of the material.

In addition to improving the humidity resistance of the materials themselves, gas pre-drying [143–146] and humidity compensation [147–150] can also enhance MOS gas sensor properties in high-humidity environments. Gas pre-drying can be achieved by evaporating [146] or condensing [143] the H_2O from mixed gases and can utilize hydrophilic sorbents, such as Nafion tubes [145], to absorb the H_2O from the sample before testing. Although gas pre-drying can alleviate humidity interference, it may remove the target VOCs, thus losing diagnostic information. An additional dehumidifying device will complicate the gas sensor and compromise its portability. Humidity compensation with reasonable algorithms [147,149,150] is also an effective strategy to reduce the hindering effects of humidity by incorporating a humidity sensor into the gas sensor system to measure the humidity levels and adjust the gas sensor's output accordingly. Humidity resistance is pivotal in gas sensor design to ensure accurate and dependable performance in practical scenarios.

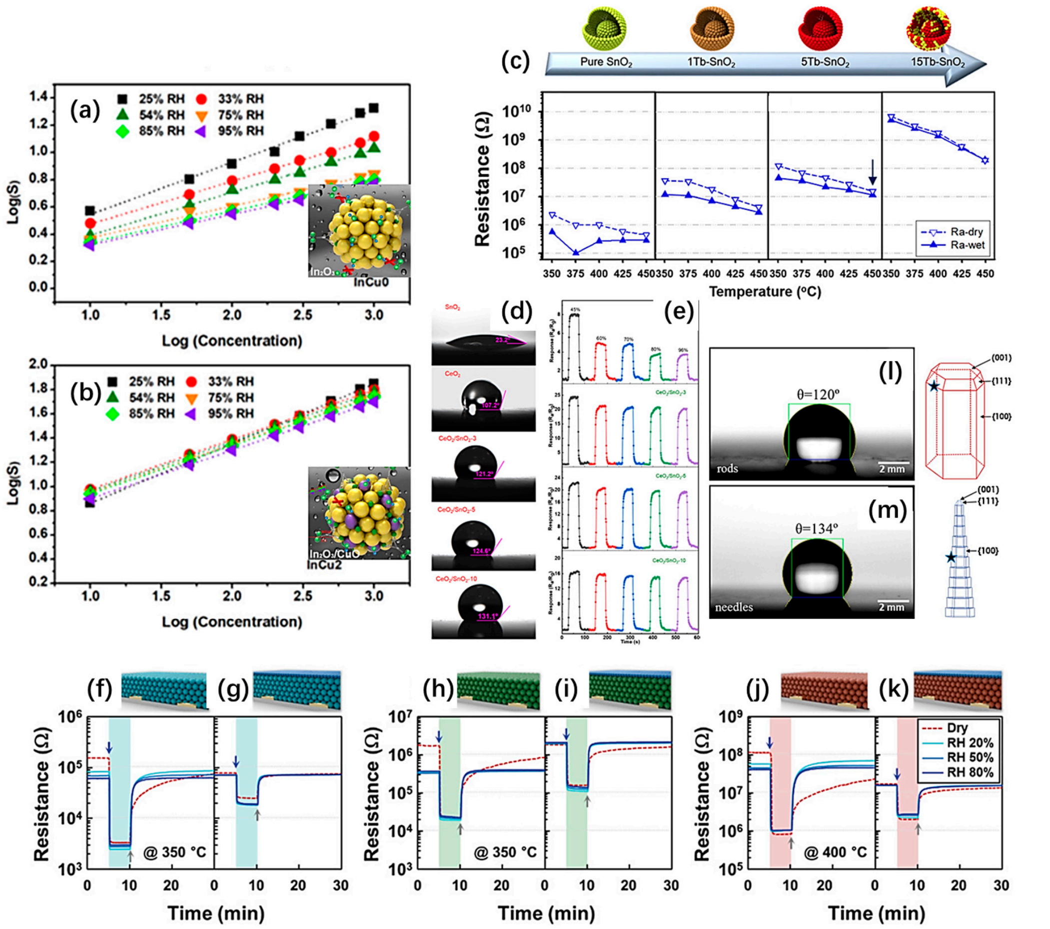

Figure 8. Improving the humidity resistance of MOS. Dynamic response and relationship between response and concentration under diverse humidity for (**a**) $InCu_0$ and (**b**) $InCu_2$. (**c**) Resistances of the pure SnO_2, 1Tb-SnO_2, 5Tb-SnO_2, and 15Tb-SnO_2 sensors under dry and 80% RH conditions. (**d**) Static water contact angle tests of SnO_2, CeO_2, and CeO_2/SnO_2 films. (**e**) Responses of SnO_2, CeO_2, and CeO_2/SnO_2 films at different RHs. Responses of pure (**f**) In_2O_3, (**h**) SnO_2, and (**j**) ZnO. Responses of (**g**) In_2O_3, (**i**) SnO_2, and (**k**) ZnO with Tb_4O_7 coverage layer. Static water contact angle tests of (**l**) rod-ZnO and (**m**) needle-ZnO. Panels (**a**,**b**): reproduced with permission from Ref. [137], © 2020 American Chemical Society. Panels (**c**): reproduced with permission from Ref. [131], © 2018 American Chemical Society. Panels (**d**,**e**): reproduced with permission from Ref. [139], © 2022 American Chemical Society. Panels (**f**–**k**): reproduced with permission from Ref. [140], © 2020 The Authors. Advanced Functional Materials published by Wiley-VCH GmbH. Panels (**l**–**m**): reproduced with permission from Ref. [142], © 2019 The Authors. Published by Elsevier B.V.

In summary, we reviewed how morphology modification and secondary modification can improve the performance of MOS gas sensors towards VOCs as lung cancer biomarkers in exhaled breath, considering the actual situation (diverse types, low concentrations, and high humidity) of exhaled breath analysis. Table 1 summarizes the latest achievements of some MOS gas-sensitive materials in detecting exhaled breath VOCs as lung cancer biomarkers.

Table 1. MOSs have been reported for potential lung cancer biomarker VOCs.

Target Gas	Material and Structure	Concentration	Temperature (°C)	Response	Res/Rec Time (s)	LOD	Interference Gas	Ref.
Benzene	Co-Al_2O_3	5/10/50 ppm	100/100/100	1.66/2.53/21.86	1.95/2.18, 2.23/2.59, 2.87/3.15	-	-	[151]
Benzene	2Rh-TiO_2/SnO_2, dual-layer sensor	5 ppm	325	35	-	-	-	[129]
Toluene	WO_3 mesoporous nanofibers	1 ppm	350	11	8.56/9.2	100 ppb	H_2, H_2S, CO, ethanol, NH_3, CH_4	[152]
Toluene	ln_2O_3	50 ppm	27	9	26/28	-	methanol, ethanol, acetone, n-butanol, and benzene	[153]
Toluene	WO_3 porous nanostructure	100 ppm	225	132	2/6	-	methanol, acetone, glycol, formaldehyde, ethanol, C_2H_2, NH_3, NO_2, and CO	[154]
Toluene	Pd-SnO_2 CNPs	1 ppb	250	3	-	200 ppt	O_2, H_2, N_2	[124]
Toluene	Pd-SnO_2 CNPs	7.9 ppb	250	15	-	7 ppt	Air	[125]
Toluene	1Rh-TiO_2/SnO_2, dual-layer	5 ppm	325	103	-	-	-	[129]
Toluene	SnO_2@SnO_2 yolk-shell cuboctahedra	20 ppm	250	28.6	1.8/4.1	-	benzene, methanol, acetone, and ethanol	[120]
Toluene	Three-, two-, one-layer hollow cubic SnO_2	20 ppm	250	38.7, 33.4, 22.1	0.8/6.1, 2.3/5.8, 2.0/6.5	-	-	[121]
Toluene	Pd-loaded SnO_2 cubic cages	20 ppm	230	41.4	0.4/16.5	100 ppb	-	[119]
Toluene	SnO_2/NiO nanoparticle	100 ppm	250	66.2	-	10 ppb	-	[155]
Xylene	0.5Rh-TiO_2/SnO_2, dual-layer	5 ppm	325	120	-	-	-	[129]
Xylene	Pt/SnO_2 nanosheet flowers	200 ppm	200	154	29/47	-	-	[156]
Xylene	Co_3O_4-SnO_2 hollow nanostructures	5 ppm	275	18.6	243/-	-	ethanol, toluene	[157]
Xylene	$CoWO_4$-Co_3O_4 heterojunctions composites	100 ppm	200	51.6	-	300 ppb	ethanol, methanol, formaldehyde, benzene, toluene, acetone, NH_3, NO_2, H_2O	[158]
Styrene	Pt-SnO_2/α-Fe_2O_3 hollow nanospheres	1 ppm	206	10.56	3/15	50 ppb	-	[159]
Isoprene	In_2O_3 nanoflowers	500 ppb	190	3.1	53/299	5 ppb	NH_3, ethanol, H_2, CO	[160]
Isoprene	ZnO quantum dots	1 ppm	350	42	42/8	10 ppb	-	[161]
Isoprene	In_2O_3/nanoparticles	1 ppm	350	231	3/35–200	1 ppb	acetone, H_2, CO_2, CO, CH_4,	[162]
Isoprene	Pt-decorated In_2O_3/microspheres	5 ppm	200	103.5	124/204	5 ppb	H_2O, CO, H_2, ethanol, ammonia	[144]
Isoprene	1 wt%Cr_2O_3/In_2O_3 nanorods clusters	500 ppb	240	1.9	135/830	5 ppb	benzene, acetone, octane, pentane, ethanol, NH_3, NO_2	[163]
Hexanal	MnO_2/$Ti_3C_2T_x$	20 ppm	100	52	134/381	-	-	[164]
Hexanal	In_2O_3 nanoparticle	50 ppm	300	18	-	-	-	[165]
Hexanal	CuO nanoflake	200 ppm	250	3.7	-	1.85 ppm	linalool, methyl salicylate	[166]
Hexanal	ZnO nanoparticle	5 ppm	250	2.12	-	-	1-pentanol, 1-octen-3-ol	[167]
Nonanal	Ru-$W_{18}0_{49}$ urchin-like	30 ppm	RT	16.1	25/154	-	SO_2, H_2S, CO, NH_3, ethanol, acetone,	[168]
Nonanal	Sb_2WO_6 hierarchical microspheres	30 ppm	RT	62	32/145	1.6 ppm	$C_8H_{16}O$, $C_9H_{14}O$, $C_6H_{12}O$, $C_{10}H_{18}O$	[169]
Nonanal	SnO_2 nanosheets	0.1/0.3 ppm	250	1.383/2	-	-	CO, NO_2, acetone, H_2, ethanol, NH_3, H_2S, formaldehyde, acetaldehyde, butanal	[170]
Butanone	Ce-SnO_2 cuboids	20 ppm	175	23.9	20/-	500 ppb	ethanol, toluene, acetone	[171]
Butanone	Pt-ZnO twin-rods	100 ppm	450	35.3	8/-	-	-	[172]

Table 1. *Cont.*

Target Gas	Material and Structure	Concentration	Temperature (°C)	Response	Res/Rec Time (s)	LOD	Interference Gas	Ref.
Butanone	Cr_2O_3/WO_3 nanosheets	100 ppm	180	40.51	9/15	-	-	[173]
Butanone	1 at% Ce-SnO_2 thin films	100 ppm	210	181	-	-	-	[174]
Butanone	ZnO small size	100 ppm	350	151	4.5/5	200 ppb	chlorobenzene, vinyl benzene, xylene, toluene, benzene, acetaldehyde, formaldehyde	[175]
Butanone	WO_3 urchin-like mesoporous	50 ppm	240	188.5	7/13	100 ppb	-	[176]
Butanone	Ag-modified NiO porous spherical	100 ppb	320	3.2	5.5/8	50 ppb	Formaldehyde, methanol, acetone, acetaldehyde	[177]
Acetone	Ru-NiO flower-like microspheres	100 ppm	200	12	71/23	-	ethanol, methanol, formaldehyde, benzene	[178]
Acetone	TiO_2/SnO_2	100 ppm	300	301.5	-	20 ppb	ethanol, acetone, NO_2	[179]
Acetone	PtCu-SnO_2	5 ppm	240	27.8	-	5 ppb	ethanol, toulene, pentane	[180]
Acetone	Pt-ZnO-SnO_2 porous nanofibers	100 ppm	170	104.26	-	-	C_7H_8, benzene, C_3H_6O	[181]
1-Propanol	Co-ZnO nanorods	100 ppm	250	491	2/19	10 ppb	formaldehyde, methyl alcohol, ethanol, triethylamine, 2-Propanol, benzene, ammonia, glacial acetic acid, formic acid	[182]
1-Propanol	$ZnSnO_3$ nanospheres	10 ppm	200	10.3	10/90	500 ppb	acetone, xylene, ammonia, hydrogen, methane	[183]
1-Propanol	ZnO/NiO one-dimensional chain MOF	500 ppm	275	280.2	31.5/18.2	200 ppb	methanol, ethanol, isopropanol, hexanol, acetone	[184]
1-Propanol	PdO-$ZnSnO_3$ hollow microspheres	100 ppm	140	30.8	1/25	-	formaldehyde, ethanol, acetone, xylene, methanol, ammonia	[185]
1-Propanol	ZnO nanoparticles	40 ppm	125	6.6	190/200	-	H_2O, ethanol, acetone, benzene, toluene	[186]
1-Propanol	Cu_2O double-shell hollow microspheres	100 ppm	187	11	50/40	10 ppm	acetone, carbon monoxide, ethyne, formaldehyde, isopropanol, ethanol, methanol	[187]
1-Propanol	NiO porous nanoparticles	20 ppb	75	1.59	-	20 ppb	ethanol, propanol, toluene, methane, NO_2	[188]
2-Propanol	10 at% Co-ZnO nanoflower	5 ppm	225	22.5	330/475	/	N_2, O_2, CO_2, acetaldehyde, isoprene, ethanol, acetone, methanol	[189]
2-Propanol	Fe-doped ZnO	250 ppb	275	4.7	51/762	250 ppb	H_2O, ethanol, acetone, methanol	[190]

2.4. Sensor Array and Pattern Recognition

This section focuses on developing the MOS gas sensor array for detecting potential lung cancer biomarkers in exhaled breath. To date, no single VOC has been identified as a specific biomarker for lung cancer [57]. Nevertheless, various highly sensitive MOS gas sensors have been developed to detect potential lung cancer biomarkers. However, detecting VOCs in exhaled breath poses significant challenges due to wide variations in composition [30], interference from other gases [32], and the low concentration of many biomarkers [25]. An ideal MOS sensor should be capable of detecting low concentrations of VOCs in the presence of high levels of interfering gases, such as water vapor, and respond rapidly to slight changes in concentration. It is difficult for a single MOS material sensor to meet all these requirements.

Inspired by biomimicry, Persaud et al. first proposed using electronic devices to mimic the olfactory system of animals in 1982, leading to the development of the e-nose [76]. The e-nose typically comprises an array of MOS gas sensors, signal acquisition, the pre-processing unit, and a pattern recognition algorithm [191]. Unlike the high selectivity of single MOS material sensors to a specific gas, each sensor in the MOS array need not have high selectivity for any given analyte. Instead, this approach records the responses between the exhaled breath and various MOSs, creating a set of specific signals known as "breath prints". Based on the existing statistical models, the "breath prints" are analyzed to recognize a range of low-concentration lung cancer biomarkers' VOCs [192]. As a simple example, Guntner et al. developed an array of five gas sensors (Figure 9a), which demonstrated excellent discrimination capabilities for mixed gases of ammonia, isoprene, and acetone [193]. Three sensors in the array were used for pattern recognition, and a simple multiple-linear-regression (MVLR) model was developed to analyze the linear response characteristics of analytes at sub-ppm concentrations (Figure 9b). Under 90% RH, the array achieved LODs of 2.9, 50.7, and 0.7 ppb for ammonia, isoprene, and acetone. These were cross-validated by the SRI-TOF-MS method, indicating the high reliability of the sensor array.

The sensor array effectively overcomes the limited selectivity of a single MOS sensor. A sensor array comprising multiple MOS gas sensors is generally required to analyze complex gases. However, using too many sensors can lead to information redundancy due to the MOS gas sensors' broad-spectrum response characteristics, increasing the difficulty of recognition systems without improving accuracy [194]. Therefore, selecting the appropriate composition of MOS sensor arrays based on specific detection requirements [195] and developing more accurate and efficient pattern recognition algorithms are necessary [194,196,197]. Principal component analysis (PCA) and linear discriminant analysis (LDA) are two of the most commonly used dimensionality reduction algorithms to improve classification accuracy, reduce computational complexity, and facilitate the visualization of output results in gas recognition.

Figure 9c depicts the response of a sensor array comprising eight MOS sensors to five VOCs related to lung cancer biomarkers [198]. By combining the PCA method, the response of each sensor is portrayed as a feature vector with arrows in PC1-PC2, successfully identifying all gases (Figure 9d). Subsequently, testing was conducted in polluted air, and the target gases were identified accurately (Figure 9e). Furthermore, after removing three sensors, the array composed of fewer sensors showed a higher resolution for acetone and methyl isobutyl ketone when tested in the same polluted air (Figure 9f), emphasizing the importance of selecting suitable sensors [195]. Li et al. projected "breath prints" of lung cancer patients and healthy individuals onto the PC1-PC2 two-dimensional space [199]. They found significant overlap between the two groups (Figure 9g), indicating little difference in the main components of the exhaled breath between lung cancer patients and healthy individuals; then, using LDA to extract the features from the two groups, the categories showed a significant distinction between the two populations (Figure 9h). Combining the features extracted by PCA and LDA showed superior identification results (Figure 9i), demonstrating the advantages of different algorithms and their combinations. These results proved the applicability of the MOS gas sensor array in lung cancer diagnosis.

To summarize, MOS gas sensor arrays offer a promising technology for simultaneously detecting and identifying multiple gases. Environmental factors, such as temperature and humidity, can affect their accuracy and reliability, which need to explore new materials and fabrication techniques. In addition to PCA and LDA, many optimized algorithms have been introduced to improve gas recognition rates [200]. Machine learning and artificial intelligence techniques are also being used to improve gas identification algorithms.

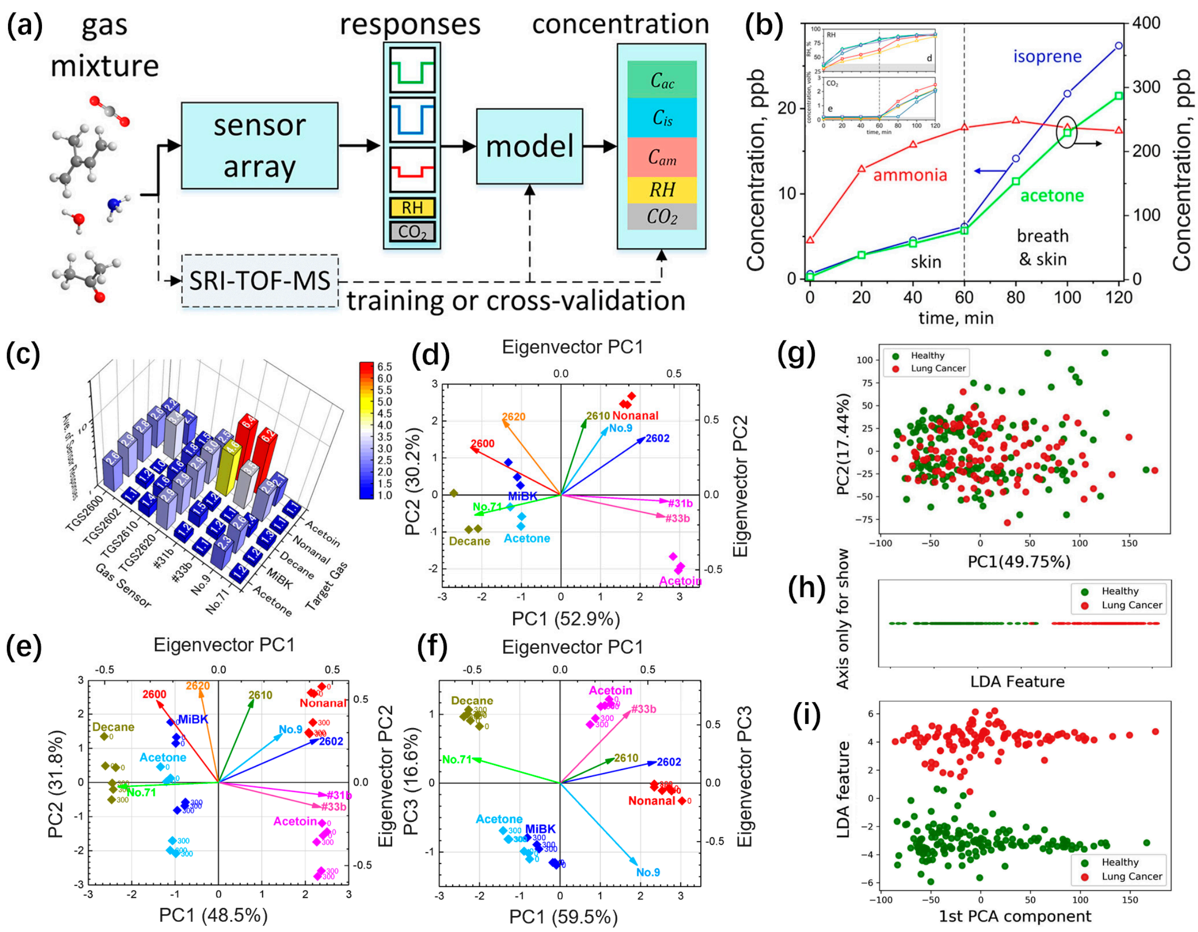

Figure 9. Sensor array and pattern recognition. (**a**) Schematic diagram of the sensor array. Each sensor individually analyzes mixed gases, and a statistical model converts their signals. Utilize SRI-TOF-MS for training or cross-validation. (**b**) Average sensor array measurements of five volunteers' ammonia, isoprene, and acetone concentrations as a function of entrapment time (the inside picture, RH, and CO_2 gas-sensing results). (**c**) Average sensor responses of eight sensors to 1 ppm of target gases in pure humid air. PCA scores and eigenvectors from (**d**) eight sensors in pure humid air, (**e**) eight sensors and (**f**) five sensors in polluted humid air. The 2D mapping results of all "breath prints" in features space, extracted by (**g**) PCA, (**h**) LDA, and (**i**) LDA with PCA. Panels (**a**,**b**): reproduced with permission from Ref. [193], © 2018 American Chemical Society. Panels (**c**–**f**) from Ref. [198]. Panels (**g**–**i**): reproduced with permission from Ref. [199], © 2020 Published by Elsevier Ltd.

3. Summary and Outlook

In recent decades, lung cancer, characterized by the highest mortality rate, has severely threatened human life and health. The primary reason for the high mortality rate is the late-stage diagnosis, emphasizing the importance of early screening. The use of exhaled breath analysis, a non-invasive, cost-effective, and user-friendly method, has been adopted to diagnose lung cancer. This article addresses the detection of VOCs in exhaled breath for early lung cancer screening using MOS gas sensors.

For a single MOS gas sensor, obtaining reasonable micro/nanostructure design and secondary modification can effectively enhance the gas sensitivity response by exposing more active sites on the MOS surface. Additionally, secondary modification is a proper technique for enhancing material selectivity. The humidity in exhaled breath can adversely affect the gas-sensing properties of MOS; therefore, this article summarizes ways to improve the humidity resistance of materials. Excellent humidity resistance composite materials can be obtained by compounding strongly hydrophilic or hydrophobic materials, low-cost doping to supplement oxygen vacancies, or exposing special crystal planes. Moreover, compared with modifying the material, pre-drying the gas before testing or using an algorithm for humidity compensation can also enhance the gas-sensing performance in a high-humidity environment.

Although the sensitivity of some single MOS gas sensors is exceptional, their broad response characteristics pose a challenge in detecting specific VOCs in exhaled breath. MOS sensor arrays can effectively address the problem of insufficient selectivity of single MOS sensors and are the future development direction of MOS gas sensing. For the analysis of more complex gases, sensor arrays comprising multiple MOS gas sensors are generally required, and efficient pattern recognition algorithms are critical to handling complex gas-sensitive information. The combination of deep learning technology and sensor arrays for detecting various diseases is an area that requires further exploration.

In summary, MOS gas sensors offer great potential for detecting human exhaled VOCs, which is significant for the early diagnosis of lung cancer on a large scale; however, several aspects require improvement:

1. Clinical diagnosis. At present, the biomarkers of the exhaled breath of lung cancer patients have not been determined, which limits the application of MOS gas sensors in diagnosing lung cancer. We urgently need a single exhaled VOC, or a unified group of VOCs, as a standard marker for lung cancer to establish a highly reliable "breath prints" comparative database, which can significantly improve the accuracy of clinical diagnosis.
2. Materials. The prerequisite for the pattern recognition of the sensor array is that MOS responds to low-concentration VOCs gas; therefore, the LOD of MOS needs to be further reduced. The high-humidity environment of exhaled breath and MOS's high-working temperature seriously affect its stability and repeatability; thus, it is necessary to develop better humidity-resistant and lower working-temperature MOS materials.
3. Algorithms. Deep learning algorithms based on olfactory recognition are needed to identify gases accurately in complex environments. Although still in its early stages, this technology has demonstrated strong recognition ability in other fields. Collaborating with sensor arrays is essential to achieve precise gas identification.
4. Devices. The collaborative design and manufacturing of gas sensors using MEMS and CMOS technology reduces their size. Multiple sensors are integrated into a sensor array, and data processing modules enable chip-level packaging and manufacturing.
5. Mechanisms. Understanding the gas-sensing mechanism involves complex chemical reactions, which are still not fully understood. Further research can improve the sensor's performance, address selectivity, and stability issues, and guide the development of gas-sensing materials.

Through the collaborative efforts of multiple disciplines, it is possible to achieve breakthroughs in all the developments mentioned above and expedite electronic noses' clinical deployment.

Author Contributions: X.L. conceived the paper; G.L. wrote the manuscript; X.Z., J.L. and S.L. prepared the original drafts. Conceptualization, X.L. and G.L.; writing—original draft preparation, X.Z.; writing—review and editing, J.L., G.L. and S.L.; visualization, X.L.; supervision, X.L.; project administration, X.L.; funding acquisition, X.L. All authors have read and agreed to the published version of the manuscript.

Funding: This research was funded by the National Natural Science Foundation of China (NSFC), grant number 22075322.

Institutional Review Board Statement: Not applicable.

Informed Consent Statement: Not applicable.

Data Availability Statement: There was no new data created or analyzed in this study. Data sharing does not apply to this article.

Conflicts of Interest: The authors declare no conflict of interest.

References

1. Bray, F.; Laversanne, M.; Weiderpass, E.; Soerjomataram, I. The Ever-Increasing Importance of Cancer as a Leading Cause of Premature Death Worldwide. *Cancer* **2021**, *127*, 3029–3030. [CrossRef] [PubMed]
2. Sung, H.; Ferlay, J.; Siegel, R.L.; Laversanne, M.; Soerjomataram, I.; Jemal, A.; Bray, F. Global Cancer Statistics 2020: GLOBOCAN Estimates of Incidence and Mortality Worldwide for 36 Cancers in 185 Countries. CA. *Cancer J. Clin.* **2021**, *71*, 209–249. [CrossRef] [PubMed]
3. Iii, C.A.P.; Burnett, R.T.; Thun, M.J.; Calle, E.E.; Krewski, D.; Ito, K.; Thurston, G.D. Lung Cancer, Cardiopulmonary Mortality, and Long-Term Exposure to Fine Particulate Air Pollution. *JAMA* **2002**, *287*, 1132–1141.
4. Detterbeck, F.C.; Chansky, K.; Groome, P.; Bolejack, V.; Crowley, J.; Shemanski, L.; Kennedy, C.; Krasnik, M.; Peake, M.; Rami-Porta, R.; et al. The IASLC Lung Cancer Staging Project: Methodology and Validation Used in the Development of Proposals for Revision of the Stage Classification of NSCLC in the Forthcoming (Eighth) Edition of the TNM Classification of Lung Cancer. *J. Thorac. Oncol.* **2016**, *11*, 1433–1446. [CrossRef]
5. Woodard, G.A.; Jones, K.D.; Jablons, D.M. Lung Cancer Staging and Prognosis. In *Lung Cancer: Treatment and Research*; Reckamp, K.L., Ed.; Cancer Treatment and Research; Springer International Publishing: Cham, Switzerland, 2016; pp. 47–75.
6. Roointan, A.; Ahmad Mir, T.; Ibrahim Wani, S.; Mati-ur-Rehman; Hussain, K.K.; Ahmed, B.; Abrahim, S.; Savardashtaki, A.; Gandomani, G.; Gandomani, M.; et al. Early Detection of Lung Cancer Biomarkers through Biosensor Technology: A Review. *J. Pharm. Biomed. Anal.* **2019**, *164*, 93–103. [CrossRef]
7. Nasim, F.; Sabath, B.F.; Eapen, G.A. Lung Cancer. *Med. Clin. N. Am.* **2019**, *103*, 463–473. [CrossRef]
8. Chen, X.; Muhammad, K.G.; Madeeha, C.; Fu, W.; Xu, L.; Hu, Y.; Liu, J.; Ying, K.; Chen, L.; Yurievna, G.O. Calculated Indices of Volatile Organic Compounds (VOCs) in Exhalation for Lung Cancer Screening and Early Detection. *Lung Cancer* **2021**, *154*, 197–205. [CrossRef]
9. Ratiu, I.A.; Ligor, T.; Bocos-Bintintan, V.; Mayhew, C.A.; Buszewski, B. Volatile Organic Compounds in Exhaled Breath as Fingerprints of Lung Cancer, Asthma and COPD. *J. Clin. Med.* **2021**, *10*, 32. [CrossRef]
10. Honnorat, J.; Antoine, J.-C. Paraneoplastic Neurological Syndromes. *Orphanet J. Rare Dis.* **2007**, *2*, 22. [CrossRef]
11. Klebe, S.; Henderson, D.W. Facts and Fiction: Premalignant Lesions of Lung Tissues. *Pathology* **2013**, *45*, 305–315. [CrossRef]
12. D'Urso, V.; Doneddu, V.; Marchesi, I.; Collodoro, A.; Pirina, P.; Giordano, A.; Bagella, L. Sputum Analysis: Non-Invasive Early Lung Cancer Detection. *J. Cell. Physiol.* **2013**, *228*, 945–951. [CrossRef]
13. Kvale, P.A.; Bode, L.F.R.; Kini, S. Diagnostic Accuracy in Lung Cancer: Comparison of Techniques Used in Association with Flexible Fiberoptic Bronchoscopy. *Chest* **1976**, *69*, 752–757. [CrossRef]
14. Visser, M.P.J.; van Grimbergen, I.; Hölters, J.; Barendregt, W.B.; Vermeer, L.C.; Vreuls, W.; Janssen, J. Performance Insights of Endobronchial Ultrasonography (EBUS) and Mediastinoscopy for Mediastinal Lymph Node Staging in Lung Cancer. *Lung Cancer* **2021**, *156*, 122–128. [CrossRef] [PubMed]
15. Raj, R.; Raparia, K.; Lynch, D.A.; Brown, K.K. Surgical Lung Biopsy for Interstitial Lung Diseases. *Chest* **2017**, *151*, 1131–1140. [CrossRef]
16. Park, S.; Jeong, W.; Moon, Y.S. X-Ray Image Segmentation Using Multi-Task Learning. *KSII Trans. Internet Inf. Syst. TIIS* **2020**, *14*, 1104–1120.
17. The National Lung Screening Trial Research Team Results of Initial Low-Dose Computed Tomographic Screening for Lung Cancer. *N. Engl. J. Med.* **2013**, *368*, 1980–1991. [CrossRef] [PubMed]
18. National Lung Screening Trial Research Team The National Lung Screening Trial: Overview and Study Design. *Radiology* **2011**, *258*, 243–253. [CrossRef]
19. Choe, W.; Chae, J.D.; Lee, B.-H.; Kim, S.-H.; Park, S.Y.; Nimse, S.B.; Kim, J.; Warkad, S.D.; Song, K.-S.; Oh, A.-C.; et al. 9G TestTM Cancer/Lung: A Desirable Companion to LDCT for Lung Cancer Screening. *Cancers* **2020**, *12*, 3192. [CrossRef] [PubMed]
20. Diaz, M.E.; Debowski, M.; Hukins, C.; Fielding, D.; Fong, K.M.; Bettington, C.S. Non-Small Cell Lung Cancer Brain Metastasis Screening in the Era of Positron Emission Tomography-CT Staging: Current Practice and Outcomes. *J. Med. Imaging Radiat. Oncol.* **2018**, *62*, 383–388. [CrossRef]
21. Abdurixiti, M.; Nijiati, M.; Shen, R.; Ya, Q.; Abuduxiku, N.; Nijiati, M. Current Progress and Quality of Radiomic Studies for Predicting EGFR Mutation in Patients with Non-Small Cell Lung Cancer Using PET/CT Images: A Systematic Review. *Br. J. Radiol.* **2021**, *94*, 20201272. [CrossRef]
22. Turner, C. Techniques and Issues in Breath and Clinical Sample Headspace Analysis for Disease Diagnosis. *Bioanalysis* **2016**, *8*, 677–690. [CrossRef] [PubMed]
23. Capuano, R.; Catini, A.; Paolesse, R.; Di Natale, C. Sensors for Lung Cancer Diagnosis. *J. Clin. Med.* **2019**, *8*, 235. [CrossRef] [PubMed]
24. Chang, J.-E.; Lee, D.-S.; Ban, S.-W.; Oh, J.; Jung, M.Y.; Kim, S.-H.; Park, S.; Persaud, K.; Jheon, S. Analysis of Volatile Organic Compounds in Exhaled Breath for Lung Cancer Diagnosis Using a Sensor System. *Sens. Actuators B Chem.* **2018**, *255*, 800–807. [CrossRef]
25. Saalberg, Y.; Wolff, M. VOC Breath Biomarkers in Lung Cancer. *Clin. Chim. Acta* **2016**, *459*, 5–9. [CrossRef] [PubMed]
26. Gordon, S.M.; Szidon, J.P.; Krotoszynski, B.K.; Gibbons, R.D.; O'Neill, H.J. Volatile Organic Compounds in Exhaled Air from Patients with Lung Cancer. *Clin. Chem.* **1985**, *31*, 1278–1282. [CrossRef]

27. Konvalina, G.; Haick, H. Sensors for Breath Testing: From Nanomaterials to Comprehensive Disease Detection. *Acc. Chem. Res.* **2014**, *47*, 66–76. [CrossRef]
28. Li, W.; Liu, H.-Y.; Jia, Z.-R.; Qiao, P.-P.; Pi, X.-T.; Chen, J.; Deng, L.-H. Advances in the Early Detection of Lung Cancer Using Analysis of Volatile Organic Compounds: From Imaging to Sensors. *Asian Pac. J. Cancer Prev.* **2014**, *15*, 4377–4384. [CrossRef]
29. Pauling, L.; Robinson, A.B.; Teranishi, R.; Cary, P. Quantitative Analysis of Urine Vapor and Breath by Gas-Liquid Partition Chromatography. *Proc. Natl. Acad. Sci. USA* **1971**, *68*, 2374–2376. [CrossRef]
30. Phillips, M.; Herrera, J.; Krishnan, S.; Zain, M.; Greenberg, J.; Cataneo, R.N. Variation in Volatile Organic Compounds in the Breath of Normal Humans. *J. Chromatogr. B. Biomed. Sci. Appl.* **1999**, *729*, 75–88. [CrossRef]
31. de Lacy Costello, B.; Amann, A.; Al-Kateb, H.; Flynn, C.; Filipiak, W.; Khalid, T.; Osborne, D.; Ratcliffe, N.M. A Review of the Volatiles from the Healthy Human Body. *J. Breath Res.* **2014**, *8*, 014001. [CrossRef]
32. Fenske, J.D.; Paulson, S.E. Human Breath Emissions of VOCs. *J. Air Waste Manag. Assoc.* **1999**, *49*, 594–598. [CrossRef] [PubMed]
33. Phillips, M.; Gleeson, K.; Hughes, J.M.B.; Greenberg, J.; Cataneo, R.N.; Baker, L.; McVay, W.P. Volatile Organic Compounds in Breath as Markers of Lung Cancer: A Cross-Sectional Study. *Lancet* **1999**, *353*, 1930–1933. [CrossRef] [PubMed]
34. Phillips, M.; Cataneo, R.N.; Cummin, A.R.C.; Gagliardi, A.J.; Gleeson, K.; Greenberg, J.; Maxfield, R.A.; Rom, W.N. Detection of Lung Cancer with Volatile Markers in the Breatha. *Chest* **2003**, *123*, 2115–2123. [CrossRef] [PubMed]
35. Phillips, M.; Altorki, N.; Austin, J.H.M.; Cameron, R.B.; Cataneo, R.N.; Greenberg, J.; Kloss, R.; Maxfield, R.A.; Munawar, M.I.; Pass, H.I.; et al. Prediction of Lung Cancer Using Volatile Biomarkers in Breath. *Cancer Biomark.* **2007**, *3*, 95–109. [CrossRef]
36. Phillips, M.; Altorki, N.; Austin, J.H.M.; Cameron, R.B.; Cataneo, R.N.; Kloss, R.; Maxfield, R.A.; Munawar, M.I.; Pass, H.I.; Rashid, A.; et al. Detection of Lung Cancer Using Weighted Digital Analysis of Breath Biomarkers. *Clin. Chim. Acta* **2008**, *393*, 76–84. [CrossRef] [PubMed]
37. Hakim, M.; Broza, Y.Y.; Barash, O.; Peled, N.; Phillips, M.; Amann, A.; Haick, H. Volatile Organic Compounds of Lung Cancer and Possible Biochemical Pathways. *Chem. Rev.* **2012**, *112*, 5949–5966. [CrossRef]
38. Preti, G.; Labows, J.N.; Kostelc, J.G.; Aldinger, S.; Daniele, R. Analysis of Lung Air from Patients with Bronchogenic Carcinoma and Controls Using Gas Chromatography-Mass Spectrometry. *J. Chromatogr. B Biomed. Sci. Appl.* **1988**, *432*, 1–11. [CrossRef]
39. Lai, X.; Cao, K.; Shen, G.; Xue, P.; Wang, D.; Hu, F.; Zhang, J.; Yang, Q.; Wang, X. Ordered Mesoporous $NiFe_2O_4$ with Ultrathin Framework for Low-Ppb Toluene Sensing. *Sci. Bull.* **2018**, *63*, 187–193. [CrossRef]
40. Ligor, T.; Ligor, M.; Amann, A.; Ager, C.; Bachler, M.; Dzien, A.; Buszewski, B. The Analysis of Healthy Volunteers' Exhaled Breath by the Use of Solid-Phase Microextraction and GC-MS. *J. Breath Res.* **2008**, *2*, 046006. [CrossRef]
41. Koureas, M.; Kirgou, P.; Amoutzias, G.; Hadjichristodoulou, C.; Gourgoulianis, K.; Tsakalof, A. Target Analysis of Volatile Organic Compounds in Exhaled Breath for Lung Cancer Discrimination from Other Pulmonary Diseases and Healthy Persons. *Metabolites* **2020**, *10*, 317. [CrossRef]
42. Schallschmidt, K.; Becker, R.; Jung, C.; Bremser, W.; Walles, T.; Neudecker, J.; Leschber, G.; Frese, S.; Nehls, I. Comparison of Volatile Organic Compounds from Lung Cancer Patients and Healthy Controls—Challenges and Limitations of an Observational Study. *J. Breath Res.* **2016**, *10*, 046007. [CrossRef]
43. Adiguzel, Y.; Kulah, H. Breath Sensors for Lung Cancer Diagnosis. *Biosens. Bioelectron.* **2015**, *65*, 121–138. [CrossRef] [PubMed]
44. Mazzone, P.J. Analysis of Volatile Organic Compounds in the Exhaled Breath for the Diagnosis of Lung Cancer. *J. Thorac. Oncol.* **2008**, *3*, 774–780. [CrossRef]
45. Amann, A.; Costello, B.d.L.; Miekisch, W.; Schubert, J.; Buszewski, B.; Pleil, J.; Ratcliffe, N.; Risby, T. The Human Volatilome: Volatile Organic Compounds (VOCs) in Exhaled Breath, Skin Emanations, Urine, Feces and Saliva. *J. Breath Res.* **2014**, *8*, 034001. [CrossRef] [PubMed]
46. Haick, H.; Broza, Y.Y.; Mochalski, P.; Ruzsanyi, V.; Amann, A. Assessment, Origin, and Implementation of Breath Volatile Cancer Markers. *Chem. Soc. Rev.* **2014**, *43*, 1423–1449. [CrossRef]
47. Barash, O.; Tisch, U.; Haick, H. Volatile Organic Compounds and the Potential for a Lung Cancer Breath Test. *Lung Cancer Manag.* **2013**, *2*, 471–482. [CrossRef]
48. Sutaria, S.R.; Gori, S.S.; Morris, J.D.; Xie, Z.; Fu, X.-A.; Nantz, M.H. Lipid Peroxidation Produces a Diverse Mixture of Saturated and Unsaturated Aldehydes in Exhaled Breath That Can Serve as Biomarkers of Lung Cancer—A Review. *Metabolites* **2022**, *12*, 561. [CrossRef]
49. Bayley, J.-P.; Devilee, P. Warburg Tumours and the Mechanisms of Mitochondrial Tumour Suppressor Genes. Barking up the Right Tree? *Curr. Opin. Genet. Dev.* **2010**, *20*, 324–329. [CrossRef]
50. Janfaza, S.; Khorsand, B.; Nikkhah, M.; Zahiri, J. Digging Deeper into Volatile Organic Compounds Associated with Cancer. *Biol. Methods Protoc.* **2019**, *4*, bpz014. [CrossRef]
51. Lunt, S.Y.; Vander Heiden, M.G. Aerobic Glycolysis: Meeting the Metabolic Requirements of Cell Proliferation. *Annu. Rev. Cell Dev. Biol.* **2011**, *27*, 441–464. [CrossRef]
52. Gashimova, E.M.; Temerdashev, A.Z.; Porkhanov, V.A.; Polyakov, I.S.; Perunov, D.V. Volatile Organic Compounds in Exhaled Breath as Biomarkers of Lung Cancer: Advances and Potential Problems. *J. Anal. Chem.* **2022**, *77*, 785–810. [CrossRef]
53. Liu, L.; Li, W.; He, Z.; Chen, W.; Liu, H.; Chen, K.; Pi, X. Detection of Lung Cancer with Electronic Nose Using a Novel Ensemble Learning Framework. *J. Breath Res.* **2021**, *15*, 026014. [CrossRef]
54. Chen, X.; Cao, M.; Li, Y.; Hu, W.; Wang, P.; Ying, K.; Pan, H. A Study of an Electronic Nose for Detection of Lung Cancer Based on a Virtual SAW Gas Sensors Array and Imaging Recognition Method. *Meas. Sci. Technol.* **2005**, *16*, 1535. [CrossRef]

55. Jia, Z.; Patra, A.; Kutty, V.K.; Venkatesan, T. Critical Review of Volatile Organic Compound Analysis in Breath and In Vitro Cell Culture for Detection of Lung Cancer. *Metabolites* **2019**, *9*, 52. [CrossRef] [PubMed]
56. Schmidt, F.; Kohlbrenner, D.; Malesevic, S.; Huang, A.; Klein, S.D.; Puhan, M.A.; Kohler, M. Mapping the Landscape of Lung Cancer Breath Analysis: A Scoping Review (ELCABA). *Lung Cancer* **2023**, *175*, 131–140. [CrossRef]
57. Miekisch, W.; Herbig, J.; Schubert, J.K. Data Interpretation in Breath Biomarker Research: Pitfalls and Directions. *J. Breath Res.* **2012**, *6*, 036007. [CrossRef] [PubMed]
58. Smolinska, A.; Hauschild, A.-C.; Fijten, R.R.R.; Dallinga, J.W.; Baumbach, J.; Schooten, F.J. van Current Breathomics—A Review on Data Pre-Processing Techniques and Machine Learning in Metabolomics Breath Analysis. *J. Breath Res.* **2014**, *8*, 027105. [CrossRef]
59. Kim, C.; Lee, K.K.; Kang, M.S.; Shin, D.-M.; Oh, J.-W.; Lee, C.-S.; Han, D.-W. Artificial Olfactory Sensor Technology That Mimics the Olfactory Mechanism: A Comprehensive Review. *Biomater. Res.* **2022**, *26*, 40. [CrossRef]
60. Peled, N.; Hakim, M.; Bunn, P.A.; Miller, Y.E.; Kennedy, T.C.; Mattei, J.; Mitchell, J.D.; Hirsch, F.R.; Haick, H. Non-Invasive Breath Analysis of Pulmonary Nodules. *J. Thorac. Oncol.* **2012**, *7*, 1528–1533. [CrossRef]
61. Yu, Q.; Chen, J.; Fu, W.; Muhammad, K.G.; Li, Y.; Liu, W.; Xu, L.; Dong, H.; Wang, D.; Liu, J.; et al. Smartphone-Based Platforms for Clinical Detections in Lung-Cancer-Related Exhaled Breath Biomarkers: A Review. *Biosensors* **2022**, *12*, 223. [CrossRef]
62. Salimi, M.; Milani Hosseini, S.M.R. Smartphone-Based Detection of Lung Cancer-Related Volatile Organic Compounds (VOCs) Using Rapid Synthesized ZnO Nanosheet. *Sens. Actuators B Chem.* **2021**, *344*, 130127. [CrossRef]
63. Di Natale, C.; Macagnano, A.; Martinelli, E.; Paolesse, R.; D'Arcangelo, G.; Roscioni, C.; Finazzi-Agrò, A.; D'Amico, A. Lung Cancer Identification by the Analysis of Breath by Means of an Array of Non-Selective Gas Sensors. *Biosens. Bioelectron.* **2003**, *18*, 1209–1218. [CrossRef] [PubMed]
64. Zhong, X.; Li, D.; Du, W.; Yan, M.; Wang, Y.; Huo, D.; Hou, C. Rapid Recognition of Volatile Organic Compounds with Colorimetric Sensor Arrays for Lung Cancer Screening. *Anal. Bioanal. Chem.* **2018**, *410*, 3671–3681. [CrossRef] [PubMed]
65. Sun, L.; Rotaru, A.; Robeyns, K.; Garcia, Y. A Colorimetric Sensor for the Highly Selective, Ultra-Sensitive, and Rapid Detection of Volatile Organic Compounds and Hazardous Gases. *Ind. Eng. Chem. Res.* **2021**, *60*, 8788–8798. [CrossRef]
66. Ji, H.; Zeng, W.; Li, Y. Gas Sensing Mechanisms of Metal Oxide Semiconductors: A Focus Review. *Nanoscale* **2019**, *11*, 22664–22684. [CrossRef] [PubMed]
67. Drmosh, Q.A.; Olanrewaju Alade, I.; Qamar, M.; Akbar, S. Zinc Oxide-Based Acetone Gas Sensors for Breath Analysis: A Review. *Chem.–Asian J.* **2021**, *16*, 1519–1538. [CrossRef] [PubMed]
68. Ahmadipour, M.; Pang, A.L.; Ardani, M.R.; Pung, S.-Y.; Ooi, P.C.; Hamzah, A.A.; Mohd Razip Wee, M.F.; Aniq Shazni Mohammad Haniff, M.; Dee, C.F.; Mahmoudi, E.; et al. Detection of Breath Acetone by Semiconductor Metal Oxide Nanostructures-Based Gas Sensors: A Review. *Mater. Sci. Semicond. Process.* **2022**, *149*, 106897. [CrossRef]
69. Raju, P.; Li, Q. Review—Semiconductor Materials and Devices for Gas Sensors. *J. Electrochem. Soc.* **2022**, *169*, 057518. [CrossRef]
70. Cheng, L.; Meng, Q.-H.; Lilienthal, A.J.; Qi, P.-F. Development of Compact Electronic Noses: A Review. *Meas. Sci. Technol.* **2021**, *32*, 062002. [CrossRef]
71. Yuan, H.; Li, N.; Fan, W.; Cai, H.; Zhao, D. Metal-Organic Framework Based Gas Sensors. *Adv. Sci.* **2022**, *9*, 2104374. [CrossRef]
72. Yang, X.; Deng, Y.; Yang, H.; Liao, Y.; Cheng, X.; Zou, Y.; Wu, L.; Deng, Y. Functionalization of Mesoporous Semiconductor Metal Oxides for Gas Sensing: Recent Advances and Emerging Challenges. *Adv. Sci.* **2023**, *10*, 2204810. [CrossRef]
73. Vajhadin, F.; Mazloum-Ardakani, M.; Amini, A. Metal Oxide-Based Gas Sensors for the Detection of Exhaled Breath Markers. *Med. Devices Sens.* **2021**, *4*, e10161. [CrossRef] [PubMed]
74. Seiyama, T.; Kato, A.; Fujiishi, K.; Nagatani, M. A New Detector for Gaseous Components Using Semiconductive Thin Films. *Anal. Chem.* **1962**, *34*, 1502–1503. [CrossRef]
75. Engelhard, E.; Gudden, B. Zur Frage Der Gültigkeit Des Ohmschen Gesetzes Bei Cu_2O. Bemerkung Zur Arbeit "Variable Widerstände Und Ihre Hydrodynamische Analogie" von R. Auerbach. *Z. Phys.* **1931**, *70*, 701–705. [CrossRef]
76. Persaud, K.; Dodd, G. Analysis of Discrimination Mechanisms in the Mammalian Olfactory System Using a Model Nose. *Nature* **1982**, *299*, 352–355. [CrossRef] [PubMed]
77. Lee, E.; Yoon, Y.S.; Kim, D.-J. Two-Dimensional Transition Metal Dichalcogenides and Metal Oxide Hybrids for Gas Sensing. *ACS Sens.* **2018**, *3*, 2045–2060. [CrossRef]
78. Das, S.; Mojumder, S.; Saha, D.; Pal, M. Influence of Major Parameters on the Sensing Mechanism of Semiconductor Metal Oxide Based Chemiresistive Gas Sensors: A Review Focused on Personalized Healthcare. *Sens. Actuators B Chem.* **2022**, *352*, 131066. [CrossRef]
79. Yamazoe, N. New Approaches for Improving Semiconductor Gas Sensors. *Sens. Actuators B Chem.* **1991**, *5*, 7–19. [CrossRef]
80. Ji, H.; Zeng, W.; Li, Y. Assembly of 2D Nanosheets into Flower-like MoO_3: New Insight into the Petal Thickness Affect on Gas-Sensing Properties. *Mater. Res. Bull.* **2019**, *118*, 110476. [CrossRef]
81. Wang, H.; Ma, J.; Zhang, J.; Feng, Y.; Vijjapu, M.T.; Yuvaraja, S.; Surya, S.G.; Salama, K.N.; Dong, C.; Wang, Y.; et al. Gas Sensing Materials Roadmap. *J. Phys. Condens. Matter* **2021**, *33*, 303001. [CrossRef]
82. Li, Z.; Yu, J.; Dong, D.; Yao, G.; Wei, G.; He, A.; Wu, H.; Zhu, H.; Huang, Z.; Tang, Z. E-Nose Based on a High-Integrated and Low-Power Metal Oxide Gas Sensor Array. *Sens. Actuators B Chem.* **2023**, *380*, 133289. [CrossRef]
83. Rath, R.J.; Farajikhah, S.; Oveissi, F.; Dehghani, F.; Naficy, S. Chemiresistive Sensor Arrays for Gas/Volatile Organic Compounds Monitoring: A Review. *Adv. Eng. Mater.* **2023**, *25*, 2200830. [CrossRef]

84. Wang, M.; Hou, T.; Shen, Z.; Zhao, X.; Ji, H. MOF-Derived Fe_2 Why $_3$: Phase Control and Effects of Phase Composition on Gas Sensing Performance. *Sens. Actuators B Chem.* **2019**, *292*, 171–179. [CrossRef]
85. Zhang, J.; Liu, X.; Neri, G.; Pinna, N. Nanostructured Materials for Room-Temperature Gas Sensors. *Adv. Mater.* **2016**, *28*, 795–831. [CrossRef] [PubMed]
86. Sahm, T.; Gurlo, A.; Bârsan, N.; Weimar, U. Basics of Oxygen and SnO_2 Interaction; Work Function Change and Conductivity Measurements. *Sens. Actuators B Chem.* **2006**, *118*, 78–83. [CrossRef]
87. Manno, D.; Micocci, G.; Rella, R.; Serra, A.; Taurino, A.; Tepore, A. Titanium Oxide Thin Films for NH_3 Monitoring: Structural and Physical Characterizations. *J. Appl. Phys.* **1997**, *82*, 54–59. [CrossRef]
88. Barsan, N.; Weimar, U. Conduction Model of Metal Oxide Gas Sensors. *J. Electroceramics* **2001**, *7*, 143–167. [CrossRef]
89. Gurlo, A. Interplay between O_2 and SnO_2: Oxygen Ionosorption and Spectroscopic Evidence for Adsorbed Oxygen. *ChemPhysChem* **2006**, *7*, 2041–2052. [CrossRef]
90. Morsy, M.; Abdel-Salam, A.I.; Mostafa, M.; Elzwawy, A. Promoting the Humidity Sensing Capabilities of Titania Nanorods/RGO Nanocomposite via de-Bundling and Maximizing Porosity and Surface Area through Lyophilization. *Micro Nano Eng.* **2022**, *17*, 100163. [CrossRef]
91. Bai, J.; Zhao, C.; Gong, H.; Wang, Q.; Huang, B.; Sun, G.; Wang, Y.; Zhou, J.; Xie, E.; Wang, F. Debye-Length Controlled Gas Sensing Performances in NiO@ZnO p-n Junctional Core–Shell Nanotubes. *J. Phys. Appl. Phys.* **2019**, *52*, 285103. [CrossRef]
92. Nakate, U.T.; Ahmad, R.; Patil, P.; Wang, Y.; Bhat, K.S.; Mahmoudi, T.; Yu, Y.T.; Suh, E.; Hahn, Y.-B. Improved Selectivity and Low Concentration Hydrogen Gas Sensor Application of Pd Sensitized Heterojunction N-ZnO/p-NiO Nanostructures. *J. Alloys Compd.* **2019**, *797*, 456–464. [CrossRef]
93. Moseley, P.T.; Norris, J.O.; Williams, D.E. *Techniques and Mechanisms in Gas Sensing*; Adam Hilger Bristol; CRC Press: Boca Raton, FL, USA, 1991; Volume 234.
94. Jain, G.H. MOS Gas Sensors: What Determines Our Choice? In Proceedings of the 2011 Fifth International Conference on Sensing Technology, Palmerston North, New Zealand, 28 November–1 December 2011; pp. 66–72.
95. Hübner, M.; Simion, C.E.; Tomescu-Stănoiu, A.; Pokhrel, S.; Bârsan, N.; Weimar, U. Influence of Humidity on CO Sensing with P-Type CuO Thick Film Gas Sensors. *Sens. Actuators B Chem.* **2011**, *153*, 347–353. [CrossRef]
96. Mohammed, R.S.; Fakhri, M.A. Titanium Dioxide–Based Sensors: A Review. *AIP Conf. Proc.* **2022**, *2660*, 020133.
97. Yan, Z.; Zhang, Y.; Kang, W.; Deng, N.; Pan, Y.; Sun, W.; Ni, J.; Kang, X. TiO_2 Gas Sensors Combining Experimental and DFT Calculations: A Review. *Nanomaterials* **2022**, *12*, 3611. [CrossRef] [PubMed]
98. Tian, X.; Cui, X.; Lai, T.; Ren, J.; Yang, Z.; Xiao, M.; Wang, B.; Xiao, X.; Wang, Y. Gas Sensors Based on TiO_2 Nanostructured Materials for the Detection of Hazardous Gases: A Review. *Nano Mater. Sci.* **2021**, *3*, 390–403. [CrossRef]
99. Hazra, A.; Das, S.; Kanungo, J.; Sarkar, C.K.; Basu, S. Studies on a Resistive Gas Sensor Based on Sol–Gel Grown Nanocrystalline p-TiO_2 Thin Film for Fast Hydrogen Detection. *Sens. Actuators B Chem.* **2013**, *183*, 87–95. [CrossRef]
100. Zhang, F.; Wang, X.; Dong, J.; Qin, N.; Xu, J. Selective BTEX Sensor Based on a SnO_2/V_2O_5 Composite. *Sens. Actuators B Chem.* **2013**, *186*, 126–131. [CrossRef]
101. Peng, G.; Tisch, U.; Adams, O.; Hakim, M.; Shehada, N.; Broza, Y.Y.; Billan, S.; Abdah-Bortnyak, R.; Kuten, A.; Haick, H. Diagnosing Lung Cancer in Exhaled Breath Using Gold Nanoparticles. *Nat. Nanotechnol.* **2009**, *4*, 669–673. [CrossRef]
102. Ferrus, L.; Guenard, H.; Vardon, G.; Varene, P. Respiratory Water Loss. *Respir. Physiol.* **1980**, *39*, 367–381. [CrossRef]
103. Bag, A.; Lee, N. Recent Advancements in Development of Wearable Gas Sensors. *Adv. Mater. Technol.* **2021**, *6*, 2000883. [CrossRef]
104. Jeong, S.-Y.; Kim, J.-S.; Lee, J.-H. Rational Design of Semiconductor-Based Chemiresistors and Their Libraries for Next-Generation Artificial Olfaction. *Adv. Mater.* **2020**, *32*, 2002075. [CrossRef]
105. Zhou, T.; Zhang, T. Recent Progress of Nanostructured Sensing Materials from 0D to 3D: Overview of Structure–Property-Application Relationship for Gas Sensors. *Small Methods* **2021**, *5*, 2100515. [CrossRef]
106. Mahajan, S.; Jagtap, S. Metal-Oxide Semiconductors for Carbon Monoxide (CO) Gas Sensing: A Review. *Appl. Mater. Today* **2020**, *18*, 100483. [CrossRef]
107. Hu, Y.; Hwang, J.; Lee, Y.; Conlin, P.; Schlom, D.G.; Datta, S.; Cho, K. First Principles Calculations of Intrinsic Mobilities in Tin-Based Oxide Semiconductors SnO, SnO_2, and Ta_2SnO_6. *J. Appl. Phys.* **2019**, *126*, 185701. [CrossRef]
108. Batzill, M. Surface Science Studies of Gas Sensing Materials: SnO_2. *Sensors* **2006**, *6*, 1345–1366. [CrossRef]
109. Ruhland, B.; Becker, T.; Müller, G. Gas-Kinetic Interactions of Nitrous Oxides with SnO_2 Surfaces. *Sens. Actuators B Chem.* **1998**, *50*, 85–94. [CrossRef]
110. Cirera, A.; Diéguez, A.; Diaz, R.; Cornet, A.; Morante, J.R. New Method to Obtain Stable Small-Sized SnO_2 Powders for Gas Sensors. *Sens. Actuators B Chem.* **1999**, *58*, 360–364. [CrossRef]
111. Li, Y.; Chen, N.; Deng, D.; Xing, X.; Xiao, X.; Wang, Y. Formaldehyde Detection: SnO_2 Microspheres for Formaldehyde Gas Sensor with High Sensitivity, Fast Response/Recovery and Good Selectivity. *Sens. Actuators B Chem.* **2017**, *238*, 264–273. [CrossRef]
112. Hwang, I.-S.; Choi, J.-K.; Woo, H.-S.; Kim, S.-J.; Jung, S.-Y.; Seong, T.-Y.; Kim, I.-D.; Lee, J.-H. Facile Control of C_2H_5OH Sensing Characteristics by Decorating Discrete Ag Nanoclusters on SnO_2 Nanowire Networks. *ACS Appl. Mater. Interfaces* **2011**, *3*, 3140–3145. [CrossRef] [PubMed]
113. Wang, B.; Zhu, L.F.; Yang, Y.H.; Xu, N.S.; Yang, G.W. Fabrication of a SnO_2 Nanowire Gas Sensor and Sensor Performance for Hydrogen. *J. Phys. Chem. C* **2008**, *112*, 6643–6647. [CrossRef]

114. Bulemo, P.M.; Cho, H.-J.; Kim, N.-H.; Kim, I.-D. Mesoporous SnO_2 Nanotubes via Electrospinning–Etching Route: Highly Sensitive and Selective Detection of H2S Molecule. *ACS Appl. Mater. Interfaces* **2017**, *9*, 26304–26313. [CrossRef]
115. Xu, Y.; Zheng, W.; Liu, X.; Zhang, L.; Zheng, L.; Yang, C.; Pinna, N.; Zhang, J. Platinum Single Atoms on Tin Oxide Ultrathin Films for Extremely Sensitive Gas Detection. *Mater. Horiz.* **2020**, *7*, 1519–1527. [CrossRef]
116. Kim, R.; Jang, J.-S.; Kim, D.-H.; Kang, J.-Y.; Cho, H.-J.; Jeong, Y.J.; Kim, I.-D. A General Synthesis of Crumpled Metal Oxide Nanosheets as Superior Chemiresistive Sensing Layers. *Adv. Funct. Mater.* **2019**, *29*, 1903128. [CrossRef]
117. Kumar, R.; Liu, X.; Zhang, J.; Kumar, M. Room-Temperature Gas Sensors Under Photoactivation: From Metal Oxides to 2D Materials. *Nano-Micro Lett.* **2020**, *12*, 164. [CrossRef] [PubMed]
118. Hong, Y.J.; Yoon, J.-W.; Lee, J.-H.; Kang, Y.C. One-Pot Synthesis of Pd-Loaded SnO_2 Yolk–Shell Nanostructures for Ultraselective Methyl Benzene Sensors. *Chem.—Eur. J.* **2014**, *20*, 2737–2741. [CrossRef]
119. Qiao, L.; Bing, Y.; Wang, Y.; Yu, S.; Liang, Z.; Zeng, Y. Enhanced Toluene Sensing Performances of Pd- Loaded SnO_2 Cubic Nanocages with Porous Nanoparticle-Assembled Shells. *Sens. Actuators B Chem.* **2017**, *241*, 1121–1129. [CrossRef]
120. Bing, Y.; Liu, C.; Qiao, L.; Zeng, Y.; Yu, S.; Liang, Z.; Liu, J.; Luo, J.; Zheng, W. Multistep Synthesis of Non-Spherical SnO_2 @SnO_2 Yolk-Shell Cuboctahedra with Nanoparticle-Assembled Porous Structure for Toluene Detection. *Sens. Actuators B Chem.* **2016**, *231*, 365–375. [CrossRef]
121. Wang, T.; Xu, H.; Wang, Y.; Zeng, Y.; Liu, B. Porous SnO_2 Triple-Shelled Hollow Nanoboxes for High Sensitive Toluene Detection. *Mater. Lett.* **2020**, *264*, 127320. [CrossRef]
122. Chen, X.; Zhao, S.; Zhou, P.; Cui, B.; Liu, W.; Wei, D.; Shen, Y. Room-Temperature NO_2 Sensing Properties and Mechanism of CuO Nanorods with Au Functionalization. *Sens. Actuators B Chem.* **2021**, *328*, 129070. [CrossRef]
123. Liu, C.; Kuang, Q.; Xie, Z.; Zheng, L. The Effect of Noble Metal (Au, Pd and Pt) Nanoparticles on the Gas Sensing Performance of SnO_2-Based Sensors: A Case Study on the {221} High-Index Faceted SnO_2 Octahedra. *CrystEngComm* **2015**, *17*, 6308–6313. [CrossRef]
124. Suematsu, K.; Harano, W.; Oyama, T.; Shin, Y.; Watanabe, K.; Shimanoe, K. Pulse-Driven Semiconductor Gas Sensors Toward Ppt Level Toluene Detection. *Anal. Chem.* **2018**, *90*, 11219–11223. [CrossRef] [PubMed]
125. Suematsu, K.; Harano, W.; Yamasaki, S.; Watanabe, K.; Shimanoe, K. One-Trillionth Level Toluene Detection Using a Dual-Designed Semiconductor Gas Sensor: Material and Sensor-Driven Designs. *ACS Appl. Electron. Mater.* **2020**, *2*, 4122–4126. [CrossRef]
126. Li, G.; Cheng, Z.; Xiang, Q.; Yan, L.; Wang, X.; Xu, J. Bimetal PdAu Decorated SnO_2 Nanosheets Based Gas Sensor with Temperature-Dependent Dual Selectivity for Detecting Formaldehyde and Acetone. *Sens. Actuators B Chem.* **2019**, *283*, 590–601. [CrossRef]
127. Kim, J.-H.; Lee, J.-H.; Park, Y.; Kim, J.-Y.; Mirzaei, A.; Kim, H.W.; Kim, S.S. Toluene- and Benzene-Selective Gas Sensors Based on Pt- and Pd-Functionalized ZnO Nanowires in Self-Heating Mode. *Sens. Actuators B Chem.* **2019**, *294*, 78–88. [CrossRef]
128. Hanh, N.H.; Duy, L.V.; Hung, C.M.; Xuan, C.T.; Duy, N.V.; Hoa, N.D. High-Performance Acetone Gas Sensor Based on Pt–Zn2SnO4 Hollow Octahedra for Diabetic Diagnosis. *J. Alloys Compd.* **2021**, *886*, 161284. [CrossRef]
129. Moon, Y.K.; Jeong, S.-Y.; Jo, Y.-M.; Jo, Y.K.; Kang, Y.C.; Lee, J.-H. Highly Selective Detection of Benzene and Discrimination of Volatile Aromatic Compounds Using Oxide Chemiresistors with Tunable Rh-TiO_2 Catalytic Overlayers. *Adv. Sci.* **2021**, *8*, 2004078. [CrossRef]
130. Jeong, S.-Y.; Moon, Y.K.; Wang, J.; Lee, J.-H. Exclusive Detection of Volatile Aromatic Hydrocarbons Using Bilayer Oxide Chemiresistors with Catalytic Overlayers. *Nat. Commun.* **2023**, *14*, 233. [CrossRef]
131. Kwak, C.-H.; Kim, T.-H.; Jeong, S.-Y.; Yoon, J.-W.; Kim, J.-S.; Lee, J.-H. Humidity-Independent Oxide Semiconductor Chemiresistors Using Terbium-Doped SnO_2 Yolk–Shell Spheres for Real-Time Breath Analysis. *ACS Appl. Mater. Interfaces* **2018**, *10*, 18886–18894. [CrossRef]
132. Egashira, M.; Nakashima, M.; Kawasumi, S.; Selyama, T. Temperature Programmed Desorption Study of Water Adsorbed on Metal Oxides. 2. Tin Oxide Surfaces. *J. Phys. Chem.* **1981**, *85*, 4125–4130. [CrossRef]
133. Großmann, K.; Wicker, S.; Weimar, U.; Barsan, N. Impact of Pt Additives on the Surface Reactions between SnO_2, Water Vapour, CO and H_2; an Operando Investigation. *Phys. Chem. Chem. Phys.* **2013**, *15*, 19151–19158. [CrossRef]
134. Singh, S.; Deb, J.; Sarkar, U.; Sharma, S. MoS_2/MoO_3 Nanocomposite for Selective NH3 Detection in a Humid Environment. *ACS Sustain. Chem. Eng.* **2021**, *9*, 7328–7340. [CrossRef]
135. Ma, N.; Suematsu, K.; Yuasa, M.; Kida, T.; Shimanoe, K. Effect of Water Vapor on Pd-Loaded SnO_2 Nanoparticles Gas Sensor. *ACS Appl. Mater. Interfaces* **2015**, *7*, 5863–5869. [CrossRef]
136. Choi, K.-I.; Kim, H.-J.; Kang, Y.C.; Lee, J.-H. Ultraselective and Ultrasensitive Detection of H_2S in Highly Humid Atmosphere Using CuO-Loaded SnO_2 Hollow Spheres for Real-Time Diagnosis of Halitosis. *Sens. Actuators B Chem.* **2014**, *194*, 371–376. [CrossRef]
137. Sun, Y.; Zhao, Z.; Suematsu, K.; Li, P.; Yu, Z.; Zhang, W.; Hu, J.; Shimanoe, K. Rapid and Stable Detection of Carbon Monoxide in Changing Humidity Atmospheres Using Clustered In_2O_3/CuO Nanospheres. *ACS Sens.* **2020**, *5*, 1040–1049. [CrossRef] [PubMed]
138. Kim, K.; Park, J.K.; Lee, J.; Kwon, Y.J.; Choi, H.; Yang, S.-M.; Lee, J.-H.; Jeong, Y.K. Synergistic Approach to Simultaneously Improve Response and Humidity-Independence of Metal-Oxide Gas Sensors. *J. Hazard. Mater.* **2022**, *424*, 127524. [CrossRef]
139. Zhu, X.; Chang, X.; Tang, S.; Chen, X.; Gao, W.; Niu, S.; Li, J.; Jiang, Y.; Sun, S. Humidity-Tolerant Chemiresistive Gas Sensors Based on Hydrophobic CeO_2/SnO_2 Heterostructure Films. *ACS Appl. Mater. Interfaces* **2022**, *14*, 25680–25692. [CrossRef] [PubMed]

140. Jeong, S.-Y.; Moon, Y.K.; Kim, J.K.; Park, S.-W.; Jo, Y.K.; Kang, Y.C.; Lee, J.-H. A General Solution to Mitigate Water Poisoning of Oxide Chemiresistors: Bilayer Sensors with Tb_4O_7 Overlayer. *Adv. Funct. Mater.* **2021**, *31*, 2007895. [CrossRef]
141. Si, Y.; Dong, Z.; Jiang, L. Bioinspired Designs of Superhydrophobic and Superhydrophilic Materials. *ACS Cent. Sci.* **2018**, *4*, 1102–1112. [CrossRef]
142. Vallejos, S.; Gràcia, I.; Pizúrová, N.; Figueras, E.; Čechal, J.; Hubálek, J.; Cané, C. Gas Sensitive ZnO Structures with Reduced Humidity-Interference. *Sens. Actuators B Chem.* **2019**, *301*, 127054. [CrossRef]
143. Peng, L.; Jiang, D.; Wang, Z.; Hua, L.; Li, H. Dopant-Assisted Negative Photoionization Ion Mobility Spectrometry Coupled with on-Line Cooling Inlet for Real-Time Monitoring H_2S Concentration in Sewer Gas. *Talanta* **2016**, *153*, 295–300. [CrossRef]
144. Han, B.; Wang, H.; Yang, W.; Wang, J.; Wei, X. Hierarchical Pt-Decorated In_2O_3 Microspheres with Highly Enhanced Isoprene Sensing Properties. *Ceram. Int.* **2021**, *47*, 9477–9485. [CrossRef]
145. Wang, Y.; Hua, L.; Li, Q.; Jiang, J.; Hou, K.; Wu, C.; Li, H. Direct Detection of Small N-Alkanes at Sub-Ppbv Level by Photoelectron-Induced O^{2+} Cation Chemical Ionization Mass Spectrometry at KPa Pressure. *Anal. Chem.* **2018**, *90*, 5398–5404. [CrossRef] [PubMed]
146. Gupta, N.; Fahad, H.M.; Amani, M.; Song, X.; Scott, M.; Javey, A. Elimination of Response to Relative Humidity Changes in Chemical-Sensitive Field-Effect Transistors. *ACS Sens.* **2019**, *4*, 1857–1863. [CrossRef] [PubMed]
147. Liu, C.; Duan, Z.; Zhang, B.; Zhao, Y.; Yuan, Z.; Zhang, Y.; Wu, Y.; Jiang, Y.; Tai, H. Local Gaussian Process Regression with Small Sample Data for Temperature and Humidity Compensation of Polyaniline-Cerium Dioxide NH_3 Sensor. *Sens. Actuators B Chem.* **2023**, *378*, 133113. [CrossRef]
148. Konvalina, G.; Haick, H. Effect of Humidity on Nanoparticle-Based Chemiresistors: A Comparison between Synthetic and Real-World Samples. *ACS Appl. Mater. Interfaces* **2012**, *4*, 317–325. [CrossRef]
149. Wang, Z.; Xie, C.; Liu, B.; Jiang, Y.; Li, Z.; Tai, H.; Li, X. Self-Adaptive Temperature and Humidity Compensation Based on Improved Deep BP Neural Network for NO_2 Detection in Complex Environment. *Sens. Actuators B Chem.* **2022**, *362*, 131812. [CrossRef]
150. Yan, M.; Wu, Y.; Hua, Z.; Lu, N.; Sun, W.; Zhang, J.; Fan, S. Humidity Compensation Based on Power-Law Response for MOS Sensors to VOCs. *Sens. Actuators B Chem.* **2021**, *334*, 129601. [CrossRef]
151. Venkatraman, M.; Kadian, A.; Choudhary, S.; Subramanian, A.; Singh, A.; Sikarwar, S. Ultra-Fast Benzene Gas (C_6H_6) Detection Characteristics of Cobalt-Doped Aluminum Oxide Sensors. *ChemistrySelect* **2023**, *8*, e202204531. [CrossRef]
152. Kim, S.-J.; Choi, S.-J.; Jang, J.-S.; Kim, N.-H.; Hakim, M.; Tuller, H.L.; Kim, I.-D. Mesoporous WO_3 Nanofibers with Protein-Templated Nanoscale Catalysts for Detection of Trace Biomarkers in Exhaled Breath. *ACS Nano* **2016**, *10*, 5891–5899. [CrossRef]
153. Dasari, S.G.; Nagaraju, P.; Yelsani, V.; Tirumala, S.; MV, R.R. Nanostructured Indium Oxide Thin Films as a Room Temperature Toluene Sensor. *ACS Omega* **2021**, *6*, 17442–17454. [CrossRef]
154. Wang, X.; Chen, F.; Yang, M.; Guo, L.; Xie, N.; Kou, X.; Song, Y.; Wang, Q.; Sun, Y.; Lu, G. Dispersed WO_3 Nanoparticles with Porous Nanostructure for Ultrafast Toluene Sensing. *Sens. Actuators B Chem.* **2019**, *289*, 195–206. [CrossRef]
155. Gao, H.; Zhao, L.; Wang, L.; Sun, P.; Lu, H.; Liu, F.; Chuai, X.; Lu, G. Ultrasensitive and Low Detection Limit of Toluene Gas Sensor Based on SnO_2-Decorated NiO Nanostructure. *Sens. Actuators B Chem.* **2018**, *255*, 3505–3515. [CrossRef]
156. Xing, Y.; Zhang, L.-X.; Li, C.-T.; Yin, Y.-Y.; Bie, L.-J. Pt Decoration and Oxygen Defects Synergistically Boosted Xylene Sensing Performance of Polycrystalline SnO_2 Nanosheet Assembled Microflowers. *Sens. Actuators B Chem.* **2022**, *354*, 131220. [CrossRef]
157. Jeong, H.-M.; Kim, J.-H.; Jeong, S.-Y.; Kwak, C.-H.; Lee, J.-H. Co_3O_4–SnO_2 Hollow Heteronanostructures: Facile Control of Gas Selectivity by Compositional Tuning of Sensing Materials via Galvanic Replacement. *ACS Appl. Mater. Interfaces* **2016**, *8*, 7877–7883. [CrossRef] [PubMed]
158. Wu, H.; Zhou, Y.; Guo, J.; Zhao, L.; Wang, T.; Yan, X.; Wang, C.; Liu, F.; Sun, P.; Lu, G. Highly Sensitive and Selective Xylene Sensor Based on P-p Heterojunctions Composites Derived from off-Stoichiometric Cobalt Tungstate. *Sens. Actuators B Chem.* **2022**, *351*, 130973. [CrossRef]
159. Liu, B.; Li, Y.; Gao, L.; Zhou, F.; Duan, G. Ultrafine Pt NPs-Decorated SnO_2/α-Fe_2O_3 Hollow Nanospheres with Highly Enhanced Sensing Performances for Styrene. *J. Hazard. Mater.* **2018**, *358*, 355–365. [CrossRef]
160. Han, B.; Wang, J.; Yang, W.; Chen, X.; Wang, H.; Chen, J.; Zhang, C.; Sun, J.; Wei, X. Hydrothermal Synthesis of Flower-like In_2O_3 as a Chemiresistive Isoprene Sensor for Breath Analysis. *Sens. Actuators B Chem.* **2020**, *309*, 127788. [CrossRef]
161. Park, Y.; Yoo, R.; Park, S.; Lee, J.H.; Jung, H.; Lee, H.-S.; Lee, W. Highly Sensitive and Selective Isoprene Sensing Performance of ZnO Quantum Dots for a Breath Analyzer. *Sens. Actuators B Chem.* **2019**, *290*, 258–266. [CrossRef]
162. Zheng, Q.; Lee, J.H.; Kim, S.-J.; Lee, H.-S.; Lee, W. Excellent Isoprene-Sensing Performance of In_2O_3 Nanoparticles for Breath Analyzer Applications. *Sens. Actuators B Chem.* **2021**, *327*, 128892. [CrossRef]
163. Wu, X.; Wang, H.; Wang, J.; Chen, J.; Shi, L.; Han, B.; Tian, X. Hydrothermal Synthesis of Flower-like Cr_2O_3-Doped In_2O_3 Nanorods Clusters for Ultra-Low Isoprene Detection. *Colloids Surf. Physicochem. Eng. Asp.* **2021**, *620*, 126606. [CrossRef]
164. Yao, Y.; Li, Z.; Han, Y.; Xie, L.; Zhao, X.; Zhu, Z. Fabrication and Characterization of a $MnO_2/Ti_3C_2T_x$ Based Gas Sensor for Highly Sensitive and Selective Detection of Lung Cancer Marker Hexanal. *Chem. Eng. J.* **2023**, *451*, 139029. [CrossRef]
165. Malara, A.; Bonaccorsi, L.; Donato, A.; Frontera, P.; Piscopo, A.; Poiana, M.; Leonardi, S.G.; Neri, G. Sensing Properties of Indium, Tin and Zinc Oxides for Hexanal Detection. In *Proceedings of the Sensors*; Andò, B., Baldini, F., Di Natale, C., Ferrari, V., Marletta, V., Marrazza, G., Militello, V., Miolo, G., Rossi, M., Scalise, L., et al., Eds.; Springer International Publishing: Cham, Switzerland, 2019; pp. 39–44.

166. Kulkarni, S.; Kummara, S.; Gorthala, G.; Ghosh, R. CuO Nanoflake-Based Sensors for Detecting Linalool, Hexanal, and Methyl Salicylate. *ACS Agric. Sci. Technol.* **2022**, *2*, 1285–1291. [CrossRef]
167. Bonaccorsi, L.; Donato, A.; Fotia, A.; Frontera, P.; Gnisci, A. Competitive Detection of Volatile Compounds from Food Degradation by a Zinc Oxide Sensor. *Appl. Sci.* **2022**, *12*, 2261. [CrossRef]
168. Zhang, C.; Xu, J.; Li, H.; Liao, H. Role of Ruthenium Incorporation on Room-Temperature Nonanal Sensing Properties of Ru-Loaded Urchin-like $W_{18}O_{49}$ Hierarchical Nanostructure. *Sens. Actuators B Chem.* **2022**, *353*, 131096. [CrossRef]
169. Zheng, Z.; Liu, K.; Xu, K.; Zhang, C. Investigation on Microstructure and Nonanal Sensing Properties of Hierarchical Sb_2WO_6 Microspheres. *Ceram. Int.* **2022**, *48*, 30249–30259. [CrossRef]
170. Masuda, Y.; Kato, K.; Kida, M.; Otsuka, J. Selective Nonanal Molecular Recognition with SnO_2 Nanosheets for Lung Cancer Sensor. *Int. J. Appl. Ceram. Technol.* **2019**, *16*, 1807–1811. [CrossRef]
171. Zhang, Y.; Wang, C.; Zhao, L.; Liu, F.; Sun, X.; Hu, X.; Lu, G. Preparation of Ce-Doped SnO_2 Cuboids with Enhanced 2-Butanone Sensing Performance. *Sens. Actuators B Chem.* **2021**, *341*, 130039. [CrossRef]
172. Oliveira, T.N.T.; Zito, C.A.; Perfecto, T.M.; Azevedo, G.M.; Volanti, D.P. ZnO Twin-Rods Decorated with Pt Nanoparticles for Butanone Detection. *New J. Chem.* **2020**, *44*, 15574–15583. [CrossRef]
173. Zhang, Q.; Xu, M.; Shen, Z.; Wei, Q. A Nanostructured Cr_2O_3/WO_3 p–n Junction Sensor for Highly Sensitive Detection of Butanone. *J. Mater. Sci. Mater. Electron.* **2017**, *28*, 12056–12062. [CrossRef]
174. Jiang, Z.; Guo, Z.; Sun, B.; Jia, Y.; Li, M.; Liu, J. Highly Sensitive and Selective Butanone Sensors Based on Cerium-Doped SnO_2 Thin Films. *Sens. Actuators B Chem.* **2010**, *145*, 667–673. [CrossRef]
175. Zhu, H.; Qin, W.; Li, J.; Yuan, Z.; Meng, F.; Shen, Y. Investigation on Butanone Sensing Properties of ZnO Sensor Under Different Calcination Temperature. *IEEE Sens. J.* **2022**, *22*, 25–32. [CrossRef]
176. Tian, Y.; Xu, D.; Liu, C.; Fang, S.; Ge, K.; Wu, Y.; Wu, M.; Liu, Q. Sea Urchin-like Mesoporous WO_3 (SUS-WO_3) for Sensitive 3-Hydroxy-2-Butanone Biomarker Detection. *Mater. Sci. Semicond. Process.* **2022**, *137*, 106160. [CrossRef]
177. Zhu, H.-M.; Qin, W.-B.; Yuan, Z.-Y.; Han, C.; Li, J.; Shen, Y.-B.; Meng, F.-L. Ppb-Level Butanone Sensor Based on Porous Spherical NiO and the Influence of Silver Modification. *Chin. J. Anal. Chem.* **2022**, *50*, 100034. [CrossRef]
178. Yang, M.; Lu, J.; Wang, X.; Zhang, H.; Chen, F.; Sun, J.; Yang, J.; Sun, Y.; Lu, G. Acetone Sensors with High Stability to Humidity Changes Based on Ru-Doped NiO Flower-like Microspheres. *Sens. Actuators B Chem.* **2020**, *313*, 127965. [CrossRef]
179. Sharma, B.; Sharma, A.; Myung, J. Highly Selective Detection of Acetone by TiO_2-SnO_2 Heterostructures for Environmental Biomarkers of Diabetes. *Sens. Actuators B Chem.* **2021**, *349*, 130733. [CrossRef]
180. Bai, J.; Shi, Y.; Liang, W.; Wang, C.; Liu, Y.; Wang, H.; Liu, F.; Sun, P.; Zhang, Y.; Lu, G. PtCu Nanocrystals with Crystalline Control: Twin Defect-Driven Enhancement of Acetone Sensing. *Sens. Actuators B Chem.* **2022**, *354*, 131210. [CrossRef]
181. Chen, L.; Song, Y.; Liu, W.; Dong, H.; Wang, D.; Liu, J.; Liu, Q.; Chen, X. MOF-Based Nanoscale Pt Catalyst Decorated SnO_2 Porous Nanofibers for Acetone Gas Detection. *J. Alloys Compd.* **2022**, *893*, 162322. [CrossRef]
182. Yuan, Z.; Li, J.; Meng, F. High Response N-Propanol Sensor Based on Co-Modified ZnO Nanorods. *J. Alloys Compd.* **2022**, *910*, 164971. [CrossRef]
183. Yin, Y.; Shen, Y.; Zhou, P.; Lu, R.; Li, A.; Zhao, S.; Liu, W.; Wei, D.; Wei, K. Fabrication, Characterization and n-Propanol Sensing Properties of Perovskite-Type $ZnSnO_3$ Nanospheres Based Gas Sensor. *Appl. Surf. Sci.* **2020**, *509*, 145335. [CrossRef]
184. Zhao, Y.; Wang, S.; Zhai, X.; Shao, L.; Bai, X.; Liu, Y.; Wang, T.; Li, Y.; Zhang, L.; Fan, F.; et al. Construction of Zn/Ni Bimetallic Organic Framework Derived ZnO/NiO Heterostructure with Superior N-Propanol Sensing Performance. *ACS Appl. Mater. Interfaces* **2021**, *13*, 9206–9215. [CrossRef]
185. Du, L.; Wang, D.; Gu, K.; Zhang, M. Construction of PdO-Decorated Double-Shell $ZnSnO_3$ Hollow Microspheres for n-Propanol Detection at Low Temperature. *Inorg. Chem. Front.* **2021**, *8*, 787–795. [CrossRef]
186. Kortidis, I.; Lushozi, S.; Leshabane, N.; Nkosi, S.S.; Ndwandwe, O.M.; Tshilongo, J.; Ntsasa, N.; Motaung, D.E. Selective Detection of Propanol Vapour at Low Operating Temperature Utilizing ZnO Nanostructures. *Ceram. Int.* **2019**, *45*, 16417–16423. [CrossRef]
187. Wang, N.; Zhou, Y.; Chen, K.; Wang, T.; Sun, P.; Wang, C.; Chuai, X.; Zhang, S.; Liu, X.; Lu, G. Double Shell Cu_2O Hollow Microspheres as Sensing Material for High Performance n-Propanol Sensor. *Sens. Actuators B Chem.* **2021**, *333*, 129540. [CrossRef]
188. Mokoena, T.P.; Swart, H.C.; Hillie, K.T.; Tshabalala, Z.P.; Jozela, M.; Tshilongo, J.; Motaung, D.E. Enhanced Propanol Gas Sensing Performance of P-Type NiO Gas Sensor Induced by Exceptionally Large Surface Area and Crystallinity. *Appl. Surf. Sci.* **2022**, *571*, 151121. [CrossRef]
189. Luo, Y.; Ly, A.; Lahem, D.; Martin, J.D.M.; Romain, A.-C.; Zhang, C.; Debliquy, M. Role of Cobalt in Co-ZnO Nanoflower Gas Sensors for the Detection of Low Concentration of VOCs. *Sens. Actuators B Chem.* **2022**, *360*, 131674. [CrossRef]
190. Luo, Y.; Ly, A.; Lahem, D.; Zhang, C.; Debliquy, M. A Novel Low-Concentration Isopropanol Gas Sensor Based on Fe-Doped ZnO Nanoneedles and Its Gas Sensing Mechanism. *J. Mater. Sci.* **2021**, *56*, 3230–3245. [CrossRef]
191. Hsieh, Y.-C.; Yao, D.-J. Intelligent Gas-Sensing Systems and Their Applications. *J. Micromech. Microeng.* **2018**, *28*, 093001. [CrossRef]
192. Broza, Y.Y.; Haick, H. Nanomaterial-Based Sensors for Detection of Disease by Volatile Organic Compounds. *Nanomedicine* **2013**, *8*, 785–806. [CrossRef]
193. Güntner, A.T.; Pineau, N.J.; Mochalski, P.; Wiesenhofer, H.; Agapiou, A.; Mayhew, C.A.; Pratsinis, S.E. Sniffing Entrapped Humans with Sensor Arrays. *Anal. Chem.* **2018**, *90*, 4940–4945. [CrossRef]

194. Tarca, A.L.; Carey, V.J.; Chen, X.; Romero, R.; Drăghici, S. Machine Learning and Its Applications to Biology. *PLoS Comput. Biol.* **2007**, *3*, e116. [CrossRef]
195. Saha, P.; Ghorai, S.; Tudu, B.; Bandyopadhyay, R.; Bhattacharyya, N. Optimization of Sensor Array in Electronic Nose by Combinational Feature Selection Method. In *Sensing Technology: Current Status and Future Trends II*; Mason, A., Mukhopadhyay, S.C., Jayasundera, K.P., Bhattacharyya, N., Eds.; Smart Sensors, Measurement and Instrumentation; Springer International Publishing: Cham, Switzerland, 2014; pp. 189–205.
196. Gardner, J.W.; Boilot, P.; Hines, E.L. Enhancing Electronic Nose Performance by Sensor Selection Using a New Integer-Based Genetic Algorithm Approach. *Sens. Actuators B Chem.* **2005**, *106*, 114–121. [CrossRef]
197. Yan, J.; Guo, X.; Duan, S.; Jia, P.; Wang, L.; Peng, C.; Zhang, S. Electronic Nose Feature Extraction Methods: A Review. *Sensors* **2015**, *15*, 27804–27831. [CrossRef] [PubMed]
198. Itoh, T.; Akamatsu, T.; Tsuruta, A.; Shin, W. Selective Detection of Target Volatile Organic Compounds in Contaminated Humid Air Using a Sensor Array with Principal Component Analysis. *Sensors* **2017**, *17*, 1662.
199. Li, W.; Jia, Z.; Xie, D.; Chen, K.; Cui, J.; Liu, H. Recognizing Lung Cancer Using a Homemade E-Nose: A Comprehensive Study. *Comput. Biol. Med.* **2020**, *120*, 103706. [CrossRef] [PubMed]
200. Rahman, S.; Alwadie, A.S.; Irfan, M.; Nawaz, R.; Raza, M.; Javed, E.; Awais, M. Wireless E-Nose Sensors to Detect Volatile Organic Gases through Multivariate Analysis. *Micromachines* **2020**, *11*, 597. [CrossRef] [PubMed]

Disclaimer/Publisher's Note: The statements, opinions and data contained in all publications are solely those of the individual author(s) and contributor(s) and not of MDPI and/or the editor(s). MDPI and/or the editor(s) disclaim responsibility for any injury to people or property resulting from any ideas, methods, instructions or products referred to in the content.